Proceedings of the 1998 U.S. DOE Hydrogen Program Review

NREL/CP-570-25315

MODELING OF BIOMASS TO HYDROGEN VIA THE SUPERCRITICAL WATER PYROLYSIS PROCESS

Robert J. Divilio
Combustion Systems Inc.
Silver Spring, MD 20910

Abstract

A heat transfer model has been developed to predict the temperature profile inside the University of Hawaii's Supercritical Water Reactor. A series of heat transfer tests were conducted on the University of Hawaii's apparatus to calibrate the model. Results of the model simulations are shown for several of the heat transfer tests. Tests with corn starch and wood pastes indicated that there are substantial differences between the thermal properties of the paste compared to pure water, particularly near the pseudo critical temperature. The assumption of constant thermal diffusivity in the temperature range of 250 to 450 °C gave a reasonable prediction of the reactor temperatures when paste is being fed.

A literature review is presented for pyrolysis of biomass in water at elevated temperatures up to the supercritical range. Based on this review, a global reaction mechanism is proposed. Equilibrium calculations were performed on the test results from the University of Hawaii's Supercritical Water Reactor when corn starch and corn starch and wood pastes were being fed. The calculations indicate that the data from the reactor falls both below and above the equilibrium hydrogen concentrations depending on test conditions. The data also indicates that faster heating rates may be beneficial to the hydrogen yield. Equilibrium calculations were also performed to examine the impact of wood concentration on the gas mixtures produced. This calculation showed that increasing wood concentrations favors the formation of methane at the expense of hydrogen.

Introduction

The Department of Energy is currently funding a research project at the University of Hawaii to produce hydrogen gas from high-moisture-content biomass using supercritical water. This work has shown that it is possible to completely gasify a paste composed of water containing 3 to 5% corn starch and 5 to 10% sawdust at supercritical conditions in a flow reactor, when an activated carbon catalyst is present. Combustion Systems Inc. has been contracted by the National Renewable Energy Laboratory (NREL) to develop a comprehensive model of this supercritical gasification process for the Department of Energy under Subcontract Number AXE-8-17103-01. This paper summarizes the status of the first seven months of work on this project.

During this time period, a comprehensive heat transfer model has been developed to calculate the temperature profiles in the University of Hawaii's reactor. A series of heat transfer tests were conducted in March 1998 in the apparatus to calibrate the heat transfer model. A literature review has been performed to identify the major reaction pathways for the pyrolysis of biomass in supercritical water. A preliminary global kinetic model has been developed to model the overall reaction pathways in the reactor. This model attempts to calculate the chemical reactions all the way from the wood feed to the gaseous products, and requires the time temperature profiles predicted by the heat transfer model. Equilibrium calculations were also performed to determine the gas compositions at chemical equilibrium and these results have been compared to the test results from the University of Hawaii's reactor when feeding a variety of materials.

Description of the University of Hawaii's SCW Reactor

The University of Hawaii has tested two configurations of their Supercritical Water Reactor (SCWR) with corn starch and wood pastes. Since the heat transfer tests were conducted using the latest configuration, this configuration will be described here. Where differences exist between the two configurations, the differences will be described using the terminology of "Old Reactor" to describe the previously tested configuration and "New Reactor" to describe the current configuration.

Figure 1 shows the overall configuration of the University of Hawaii's new reactor. The University of Hawaii's Supercritical Water Reactor consists of a Hastelloy tube that is 9.53 mm (0.375 inches) OD by 6.22 mm (0.245 inches) ID which is heated at the inlet by an entrance heater and by a annular heater inside the reactor pipe. Both heaters are electrical heaters that consist of a resistance heating element installed inside of an Inconel 600 sheath. The entire reactor is placed inside of a three-zone tube furnace. During the heat transfer tests, described later, thermocouples were attached to the tube wall at the positions indicated in Figure 1. The thermocouples located both inside the furnace and outside of the furnace were held in place using metal hose clamps. The three thermocouples located in the Entrance Heater block were sandwiched between the block and the tube wall.

Figure 2 shows the entrance region of the new reactor in expanded detail. The Entrance Heater consists of two 63.5 mm (2.5 inches) long steel blocks which fit together to form a round casing that is 25.4 mm (1 inch) OD and 9.53 mm (0.375 inches) ID and fits over the reactor wall at the entrance of the electrically heated furnace. Heat is supplied to this block by a 4.76 mm (3/16 inch) OD by 127 cm (50 inches) long heating element that is coiled around the outside of the Entrance Heater blocks.

In addition to the entrance heater, the SCWR Reactor is also heated by an Annulus Heater that runs down the center of the tube. In the old reactor configuration, the Annulus Heater entered the reactor from the upstream side and extended 15.24 cm (6 inches) inside the furnace. In the new reactor configuration, the Annulus Heater enters from the down stream end of the reactor, forming an annular space for fluid flow along the entire length of the reactor. The Annulus Heater is 3.18 mm (1/8 inch) OD. The heater in the old reactor had a heated length of 15.24 cm (6 inches) which started at the entrance of the Entrance Heater block. The Annulus Heater in the new reactor has a heated length of 25.4 cm (10 inches), and is positioned as shown in Figures 1 and 2.

Both the Entrance Heater and the Annulus Heater are located inside of an electrically heated furnace. The furnace has three zones, shown in Figure 1, which are independently controlled to maintain a constant temperature. Normally, during a test, all three zones are set to maintain the same temperature. Generally, the Entrance Heater and the Annulus Heater supply sufficient heat to heat the reactants flowing in the reactor up to test temperatures, so that the furnace simply prevents heat loss from the reactor walls.

An exit heater is also located at the down stream end of the furnace. The Exit Heater is similar in construction to the Entrance Heater. The primary function of the exit heater is to prevent heat loss from the down stream portion of the furnace.

Heat Transfer Model

The Heat Transfer model involves a differential energy balance around an element of the flowing fluid and a second differential energy balance around an element of the reactor wall. The two differential energy balances are coupled by the boundary conditions at the fluid-wall interface, which state that the heat flux through the wall is equal to the heat flux into the fluid.

Fundamental Equation - Heat Transfer to Fluid

A differential energy balance, in cylindrical coordinates for heat transfer to a fluid flowing in a pipe yields the following differential equation:

$$\left[\frac{\partial^2 t}{\partial r^2}+\frac{1}{r}\frac{\partial t}{\partial r}\right]=\frac{u_x}{\alpha}\frac{\partial t}{\partial x} \qquad (1)$$

Where: t = temperature, °C

r = radius, m

x = distance from the inlet of the pipe, m

u_x = velocity along the length of the pipe, m/sec

$\alpha = \frac{k}{\rho C_p}$, thermal diffusivity, m^2/sec

k = thermal conductivity of fluid Watt/m °C

r = density of fluid, g/m^3

C_p = specific heat of fluid, Joule/g °C

Equation 1 is subject to boundary conditions that specify the location and type of the heating or cooling surfaces. The velocity, u_x, in Equation 1 is also a function of radial position. For a pipe with no internal elements, the velocity profile is generally parabolic, and the velocity is given by:

$$u_x = 2u_b\left[1-\left(\frac{r}{R_o}\right)^2\right] \qquad (2)$$

Where: u_b = the average velocity in the pipe at distance x.

For flow through an annulus, the velocity profile is given by:

$$u_x = \frac{4u_b}{2R_{max}^2 - R_o^2 - R_i^2}\left[r^2 - R_o^2 - R_{max}^2 \ln\left(\frac{r}{R_o}\right)\right] \qquad (3)$$

Where: $R_{max} = \sqrt{\frac{R_o^2 - R_i^2}{2\ln(R_o/R_i)}}$

Ro = inside radius of the reactor wall.

Ri = outside radius of the annulus

Equations 1, 2, and 3 were solved using a Crank-Nicholsen Finite Difference method (Chapra 1988).

Fundamental Equation - Heat Conduction to Tube Wall

Because of the high pressures used in the University of Hawaii's SCWR, the tube wall is relatively thick. This results in considerable heat conduction both in the radial direction as well as in the axial direction. To account for this heat conduction, a separate heat balance must be performed for the tube wall. The fundamental equation governing heat transfer and conduction in the tube wall is:

$$\frac{\partial^2 T}{\partial r^2} + \frac{1}{r}\frac{\partial T}{\partial r} + \frac{\partial^2 T}{\partial x^2} = 0 \qquad (4)$$

Equation 4 is also applicable to the heat transfer in the Entrance Heater Block. Note that Equation 4 also accounts for axial heat dispersion with the last term. This term was not included in Equation 1 above, because it was assumed that the flowing fluid makes the axial heat dispersion in the liquid negligible compared to the radial heat transfer. This equation is coupled to Equation 1 by boundary conditions at the inside of the tube wall. This coupling is accomplished in the numerical solution by setting heat flux through the wall equal to the heat flux through the fluid. Solution of Equation 4 was performed using an explicit centered finite difference method with Gausian elimination

Boundary Conditions

Figure 3 shows the boundary conditions applied to the system of equations defined by Equations 1 through 4. The integration is performed from 2 inches upstream of the entrance heater to one inch beyond the end of the annulus heater. No attempt was made to model the heat transfer in the catalyst bed or at the Exit Heater, because the data and the model results showed that the temperature profile was relatively flat and up to the test temperature by the time the fluid enters the catalyst bed.

The fluid enters two inches upstream of the entrance heater at a constant temperature, T_O. Heat is transferred from the ambient air to the wall of the reactor tube via convection. To model the resistance heater that is wrapped around the entrance heater block, a constant temperature, T_B, is applied to the outside edge of the entrance heater block. Because the edge of the Entrance Heater block that faces the outside of the furnace is insulated, a zero heat flux is applied to this face. Inside the furnace, heat transfer is governed by both convection and radiation to both the wall of the reactor and to the inside face of the Entrance Heater block. A constant heat flux is applied to the wall of the heated portion of the Annulus Heater. The unheated portion of the annulus has a zero heat flux, as does the center line of the reactor upstream of the entrance heater.

The heat balance to the Entrance Heater block is coupled to the heat balance to the tube wall by the boundary conditions at the interface between the two pieces of metal. At this interface, the heat flux through the tube wall will be equal to the heat flux through the entrance heater block times a contact factor, α_c, which specifies the contact efficiency between the two pieces of metal ($0 < \alpha_c < 1.0$). This is expressed as:

$$q_m = \alpha_c q_b \qquad (5)$$

or:

$$k_m \frac{T_{(x,zz)} - T_{(x,zz-1)}}{\Delta R_m} = \alpha_c k_b \frac{T_{(x,zz+1)} - T_{(x,zz)}}{\Delta R_b} \quad (6)$$

Where the subscript "m" refers to the properties of the tube wall, the subscript "b" refers to the properties of the entrance heater block, and zz is the node at the interface between the entrance heater blocks and the tube wall.

At the fluid/metal interface, the heat flux through the metal is equal to the heat flux to the fluid as recommended by Parankar 1980. This couples the temperature distribution of the fluid to the temperature distribution of the metal. This is expressed as:

$$k \frac{T_{(x,M)} - T_{(x,M-1)}}{\Delta R} = k_m \frac{T_{(x,M+1)} - T_{(x,M)}}{\Delta R_m} \quad (7)$$

Solution of Equations 1 through 7 is accomplished as follows. First the temperature profile is assumed. Equations 1, 2, 3 and 7 are used to solve for the fluid temperatures using the assumed wall temperature profile. Next, Equations 4, and 6 are used to solve for the temperature profile through the reactor wall and in the Entrance Heater block, using the fluid temperature profile that was previously calculated. The calculation then iterates between the solution for the fluid and the solution for the wall temperatures until the calculation converges to a solution. Convergence criteria are set at 0.001 °C for successive iterations for all temperatures in the reactor wall.

Heat Transfer Tests

On March 10 and 11, 1998, a series of tests were conducted to develop the data necessary to calibrate the heat transfer model. Table 1 lists the tests that were conducted.. Tests 1, 2, and 3 consisted of operating each heater element at two different power settings while keeping the other heaters off. The final three tests used combinations of the heaters at power settings typical of the settings used during the gasification tests.

Table 1. Heat Transfer Test Matrix
Test Dates: March 10 and 11, 1998

Test Number	Entrance Heater, %	Annulus Heater, %	Furnace Temp. °C
1A	15	0	Off
1B	30	0	Off
2A	0	10	Off
2B	0	20	Off
3A	0	0	500
3B	0	0	650
4	30	0	650
5	30	20	650
6	30	35	650

Figure 4 shows the temperature profiles obtained for the nine tests listed in Table 1. Also shown in Figure 4 are the relative locations of the Entrance Heater, the heated and unheated portions of the Annulus Heater the catalyst bed, and the exit heater. The data in this figure was used to calibrate the heat transfer coefficients in the Heat Transfer Model.

Model Results

Figures 5 through 9 show the results of the Heat Transfer Model simulations of Tests 3A, 3B, 4, 5, and 6. All four figures contain two graphs which show the axial and the radial temperature profiles calculated by the model. The axial temperature profile graph shows the temperatures along the length of the reactor from 2 inches upstream of the entrance heater block to 11 inches inside the furnace. The data points obtained for the test are plotted on this graph. The heavy solid line on the axial temperature profile graph is the average temperature of the fluid, averaged radially. The heavy dashed line is the average wall temperature of the reactor tube, also averaged radially. The heavy double dashed line is the temperature at the surface of the annulus heater. In addition to those lines, three light dashed lines show the temperature at radii of 2.4 mm, 2.7 mm, and 2.9 mm. The heavy shaded line is the average temperature profile of the Entrance Heater block, averaged radially. The curves on the radial temperature profile graph give the temperature profile in the vicinity of the temperature probes that were attached to the reactor walls. The temperatures are plotted for both the fluid (from 0 to 3.1 mm) and for the reactor tube wall (>3.1 mm). Temperatures of the Entrance Heater block are not shown on this graph.

Figures 5 through 9 show that the model does a reasonable job of predicting the wall temperatures, with the exception of two thermocouples. The first is located outside of the furnace, 1 inch up-stream of the entrance heater. The second is the thermocouple located in the middle of the entrance heater block. We are currently looking at ways to modify the model to improve the temperature predictions in these two areas. However, it is quite likely that these readings are the result of non-ideal geometry's and may not be modeled accurately.

The basic features observed in Figures 5 through 9 can be explained by looking at the quantity of heat necessary to raise the water temperature up to a desired temperature. Figure 10 shows the results of this calculation for the test conditions used during the heat transfer tests. This figure shows that between 375 and 425 °C, there is a dramatic change in the quantity of heat that must be absorbed by the water in order to increase the temperature. The dashed line in Figure 10 shows the quantity of heat that would need to be absorbed, if the heat capacity of the fluid remained constant. The heat absorption in this temperature range is indicative of a phase change, although the water is supercritical and there is no phase change. This "Pseudo Boiling" phenomena is caused by the fact that at 395 °C, the heat capacity of the water at 28 MPa is about 7.5 times the heat capacity at either 200 °C or at 500 °C. Thus, in order for the water to heat above this temperature range, an additional quantity of heat must be absorbed. This causes the axial temperatures around 500 °C to flatten out as the radial temperatures begin to diverge. Figure 9 shows that once this region is passed, the temperatures again rise rapidly as additional heat is applied.

Heat Transfer to Wood-Paste Mixtures

Figure 11 shows the wall temperature profile measured on December 29, 1997. Two wall temperature profiles are shown in this figure. The thin line is the wall temperature profile obtained when feeding water just prior to the wood feed. The second is the wall temperature profile when feeding a mixture of 10.5 wt. % poplar wood and 4 wt. % potato starch in water. This data show that, unlike the water, the wood paste mixture does not experience the axial wall temperature flattening in the region of 500 °C. Instead, the wall temperature rapidly rises to 700 °C and remains relatively flat after that. This indicates that the thermal properties of the wood paste mixture are considerably different than the thermal properties of pure water, particularly in the region of the pseudo critical point.

Figure 12 shows the results of the Heat Transfer Model when the thermal diffusivity is assumed to be constant in the temperature range 250 to 450 °C. The conditions of this figure were the same as the operating conditions of Test 5. This figure shows the same wall temperature trends as observed in the paste data in Figure 11. However, more data will be needed to verify the assumptions made in this calculation.

Figure 13 shows the same data in Figure 12 plotted as a function of time in the reactor, based on the average velocity of the fluid. This plot shows that the fluid takes approximately 40 seconds to enter the heated portion of the furnace. At that point, the average fluid temperature is about 200 °C, while the fluid at the wall is near 400 °C. The fluid takes an additional 20 seconds before it reaches the catalyst bed. Furthermore, it is over 600 °C for almost 12 seconds before reaching the catalyst bed. Fluid temperatures near the annulus can be over 750 °C for as much as eight seconds.

Kinetic Model

The second task of this project was to develop a kinetic model of the supercritical water pyrolysis process. The first step in the development of this model was to perform a literature review of the data on pyrolysis in supercritical water. This review has also been expanded to include supercritical water oxidation (SCWO), as some of the reactions in SCWO are also applicable to the pyrolysis process.

Pyrolysis of biomass in supercritical water is quite rapid. In fact, as the heat transfer model showed, by the time the reaction products are brought up to the test temperature and reach the catalyst bed (about 20 seconds in the new reactor configuration), most of the primary gasification reactions will have been completed. Therefore, a kinetic model of the University of Hawaii's reactor will require a model that is capable of following the chemistry of the reaction from room temperature up to the test temperature. Modeling of the University's apparatus is further complicated by the fact that the only chemical measurements are made on the gas products collected at the exit of the reactor. Critical chemical measurements at the front end of the reactor, where most of the chemical reactions occur, are impossible with this type of reactor.

Literature Review

Supercritical water possesses some unique characteristics that are beneficial to the water-biomass pyrolysis chemistry. Figure 14 shows the hydrogen ion concentration in pure water as a function of temperature and pressure (Marshall 1981). This figure shows the calculated hydrogen ion concentration of water as a function of temperature at pressures of 20.8, 28.0 and 34.6 MPa. This figure shows that the hydrogen ion concentration in water at 250 °C is about 25 times greater than the hydrogen ion concentration at room temperature (10^{-7} mol/L at room temperature). However, above the pseudo critical temperature, the hydrogen ion concentration rapidly drops to several orders of magnitude below the concentration at room temperature. Holgate (1994) concluded that the "... operating conditions of supercritical water oxidation process are not readily able to support ionic chemistry, and that the oxidation process most likely occurs through free radical pathways".

Therefore, reactions that follow a temperature-time profile such as the one shown in Figure 13 will first experience high hydrogen ion concentrations and will be subject to acid catalyzed reactions, such as dehydration of glucose compounds, and will then quickly pass into a reaction regime that favors free radical chemistry. Note that char formation is one such acid catalyzed reaction. Antal (1997) has reported the formation of plugs in the entrance region of their apparatus at the University of Hawaii when feeding wood or sewage sludge. No such plugs were encountered when feeding glucose or corn starch. This would tend to suggest that the plug is a char formation that is caused by acid catalyzed reactions with lignin or lignin decomposition products.

Numerous articles have been published related to the hydrothermal reactions of biomass, particularly at low temperatures (less than 300 °C). An excellent review of the literature on this subject can be found in Bobleter (1994). Hydrothermal processes were generally developed to recover chemicals such as sugars and cellulose fibers from biomass. A variety of processes have been developed to take advantage of the water-biomass chemistry at low temperatures. At these conditions, the basic components of biomass, cellulose, hemicellulose and lignin, behave differently, depending on whether they have been isolated from the wood matrix. As such, this discussion will concentrate on whole biomass experiments.

Bobleter's (1994) discussion of hydrothermal biomass treatment processes can be summarized as follows:

- In the temperature range of 180-220 °C and with short reaction times
  - hemicelluloses (polyoses) can be dissolved in water
  - some lignin will also be extracted
  - the degree of polymerization (DP) of the cellulose decreases with increasing time and temperature.

- In the temperature range 280-300 °C cellulose is also rapidly decomposed to low molecular weight products.

- Cellulose was found to decompose according the following mechanism:

$$\text{Cellulose} \xrightarrow[H_2O]{k_1} \text{glucose} \xrightarrow{k_2} \text{decomposition products}$$

  Over a wide temperature range cotton cellulose follows a first order decomposition with an activation energy E_1 = 129.1 kJ/mol (Schwald 1989). Other cellulose products showed similar activation energies, however the reaction rate constants differed.

- During hydrothermal treatment of biomass, the pH of the water solution increases up to a maximum of about 3.0. However, this pH change does not appear to have a significant effect on the reaction rate.

- The activation energy for the acid hydrolysis of hemicellulose is in the range of 106 to 160 kJ/mol (Bobleter 1994). The activation energy for the thermal hydrolysis of hemicellulose can be expected in this same range.

- Delignification of biomass under hydrothermal conditions is most likely the result of α-aryl ether hydrolysis which has an activation energy of about 80 kJ/mole (Sarakanen 1981).

Insight into the biomass pyrolysis can also be inferred from the literature on glucose pyrolysis in supercritical water. However, it should be stressed that glucose is only one of several sugars that are formed during the thermal hydrolysis of biomass. Furthermore, decomposition of lignins result in compounds, such as monomeric phenols that are expected to behave quite differently than glucose. Holgate (1995) studied the reaction products formed in the temperature range of 425 to 600 °C for the pyrolysis of glucose. Holgate's data is presented in Figure 15 for an initial glucose concentration of 1.02×10^{-3} mol/L and a 6.1 second residence time at a pressure of 246 bar. At 425 °C, the major reaction products were found to be acetic acid, acetonylacetone, 5-hydroxymethylfurfural (5HMF), furfural, and propenoic acid. Above 575 °C, the only reaction products were hydrogen, carbon dioxide, methane, and a small amount of ethane.

The authors of the study indicated that ethylene may also be present at the higher temperatures, and stated that analytical error may be the cause for the disappearance of ethylene at 575 and 600 °C. Xu (1996) also observed ethylene in their gas products even at 600 °C. Xu's data show that the ratio of ethane to ethylene ranged from 4.38 at 500 °C to 10 at 550 °C and increased to 31.25 at 600 °C. Holgate (1995) postulated that the glucose pyrolysis mechanism proceeds via the fast formation of intermediate compounds followed by secondary reactions to form lighter gases, which then degrade to the final reaction products.

The data in Figure 15 show several other interesting features as well. Hydrogen, carbon dioxide and carbon monoxide begin to appear between 425 and 450 °C and are released in equal proportions up to about 500 °C. However above 500 °C, their yields begin to diverge, indicating the start of another reaction mechanism, which the authors of the study termed a "Fast water-gas-shift-type pathway". Methane and ethane both appear to begin forming between 475 and 500 °C and show comparable formation trends

The data in Figure 12 can be explained by two competing intermediate pathways and a third high temperature pathway. One intermediate temperature pathway proceeds through the formation of acetic acid, which ultimately forms CO, CO_2, and H_2, in roughly equal molar amounts and a small amount of methane. The second intermediate temperature pathway proceeds through the formation of propenoic acid, which ultimately forms CO, CO_2, and H_2, again in roughly equal molar proportions and a small amount of ethylene, which reacts with hydrogen to form ethane. The high temperature pathway proceeds via the formation of unstable free radicals which react with water to form CO_2 and H_2 in approximately a molar ratio of 2 moles of H_2 per mole of CO_2 formed.

Comparison of Holgate's (1995) data to Xu's (1996) data also show a concentration effect on the gasification efficiency. Holgate's data showed 100% gasification of 0.001 mol/L glucose at 575 °C and 600 °C after only 6 seconds of residence time. Xu's data indicated only 80% carbon gasification efficiency for 1.2 mol/L glucose at 600 °C after 34 seconds of residence time. Xu needed a carbon catalyst to achieve 100% gasification in their apparatus. It is likely that the higher glucose concentrations in Xu's data resulted in the formation of more light compounds, such as acetic acid, which are quite stable in supercritical water at these conditions. There may also be a pressure effect, as Holgate's data was taken at 24.6 MPa while Xu's data was taken at 34.5 MPa.

The parallel reaction pathways between the formation of propenoic acid and acetic acid will ultimately determine the ratio of methane to ethane from the intermediate temperature reaction pathways. Webley and Tester (1991) indicated that ethane is also formed during supercritical water oxidation conditions by radical recombination of methyl radicals, which will be formed by the high temperature pathway. The ratio of methane to ethane was relatively unaffected by temperature between 500 and 600 °C and averaged 3.6 in Xu's data for a 1.0 mol/L glucose solution, while Holgate's data show higher ratios with considerable scatter. In Holgate's data, the average ratio of methane to ethane over the temperature range of 500 to 600 °C was 10.0 and ranged from a low of 5.7 at 525 °C to a high of 17.5 at 600 °C for the lower concentrations of 0.001 mol/L of glucose (the actual ratios were: 10.0 at 500 °C; 5.7 at 525 °C; 8.0 at 550 °C; 8.75 at 575 °C; and 17.5 at 600 °C, however the authors indicated that there was considerable error in the measurement of ethane for the high temperature tests, which will impact these ratios dramatically, given the low levels of methane and ethane encountered).

One model compound for lignin pyrolysis in supercritical water that has been studied is *1,3*-Butanediol (West 1987). West studied the pyrolysis of *1,3*-Butanediol at 425 °C both with and

without the presence of water. She found that the reaction in supercritical water altered the selectivity of the reactions to give mainly propene and formaldehyde. Significant amounts of hydrogen were not formed at this temperature, which is consistent with Holgate's findings for glucose. However, CO2 was formed in significant quantities, unlike Holgate's data for glucose. West also found that the role of trace quantities of oxygen in the supercritical reaction mixture was to serve as an inhibitor to the overall conversion of *1,3*-Butanediol. She also concluded that the dielectric constant and low hydrogen ion concentration of the supercritical water suppressed the formation of char by reducing dehydration and subsequent condensation or polymerization reactions.

Proposed Reaction Mechanism

While it is not possible to identify all of the reaction mechanisms that occur during the supercritical water pyrolysis of biomass, the literature suggests the following overall reaction pathways. As the reactants begin to heat up, the hemicellulose and the lignin fractions of the wood will begin to hydrolyze and dissolve into solution. This reaction begins to occur at a reasonable rate at temperatures as low as 180 °C, which as Figures 12 and 13 show begins outside of the furnace. As long as the temperature is low enough to support ionic mechanisms, the decomposed hemicellulose will begin to react with the lignin fragments to from char. As the temperature increases further, the cellulose will also begin to decompose into glucose fragments, and these will further decompose to lighter compounds. By the time the fluid reaches the pseudo critical temperature (395 °C at 28 MPa) all of the biomass will have been dissolved into compounds of length C5 and C6 along with their decomposition products (secondary reaction products), especially acetic acid and propenoic acid. At this point, the reaction mechanisms shift from ionic reactions to free radical reactions. Hydrogen, carbon dioxide, and carbon monoxide will begin to evolve at this point in roughly equal molar ratios. Methane and ethane begin to appear around 475 °C either from the decomposition of acetic acid and propenoic acid or through radical recombinations of methyl radicals. Around 500 °C, the free radical reactions begin to dominate the chemistry. Carbon monoxide formation decreases and hydrogen and carbon dioxide begins to form in a molar ratio of roughly 2 moles of hydrogen to one mole of carbon dioxide.

The time-temperature history of the reaction products is critical to the proposed mechanism. For example, acetic acid is quite stable in supercritical water. Xu (1996) gasified acetic acid in their apparatus at the University of Hawaii at 600 °C and 34.5 MPa both with and without the carbon catalyst. Without the carbon catalyst, they achieved a gasification efficiency of 51% after 27 seconds of a 0.1 M solution of acetic acid. With the carbon catalyst, they achieved 82% gasification efficiency. Furthermore, the ratio of H_2 to CO_2 in these tests was 1.3 for the test without the catalyst and 1.0 with the catalyst. Thus, if the upstream temperatures favor the formation of acetic acid, by keeping the reaction in the intermediate temperature range longer, then the yield of hydrogen will suffer.

Equilibrium Considerations

Once the gas products of H_2, CO_2, CO, CH_4 and C_2H_6 are formed by the secondary gasification reactions, they will continue to react according to two reversible tertiary reactions. The first is the water-gas shift reaction:

$$CO + H_2O \Leftrightarrow CO_2 + H_2 \tag{8}$$

and the second is the Methane Formation Reaction:

$$CO + 3H_2 \Leftrightarrow CH_4 + H_2O \tag{9}$$

Because Equations 8 and 9 are reversible reactions, they can be driven in either direction, depending on the concentrations of the reacting species. For example, removing CO_2 from the reaction products will cause higher hydrogen yields as the concentrations of the species in Reaction 8 adjust to the equilibrium ratio given by:

$$\frac{[CO^*][H_2O^*]}{[CO_2^*][H_2^*]} = K_{eq}^{WG} = 10^{1.416} e^{-\frac{3432.5}{T}} \tag{10}$$

In fact, this is the basis for the Sorption Enhanced Reaction process for the production of hydrogen (Sircar 1998).

As a first step in the analysis of the data from the University of Hawaii, HYSIM was used to calculate the theoretical equilibrium concentrations of H_2, CO_2, CO, CH_4 and C_2H_6 that would be expected at the conditions of their tests. Figure 16 shows the flow sheet used for the HYSIM simulation. The feed is composed of carbon, hydrogen and oxygen, contained in the wood and corn starch, and water in the proportions of the feed for each test period. This feed stream is fed to a Gibbs reactor, which calculates the equilibrium concentrations at the temperature and pressure of each test by minimizing the Gibbs Free Energy of the mixture. The equilibrium products are then cooled to 25 °C and 1 atmosphere pressure and fed to a gas/liquid separator which performs a flash calculation to determine the quantity and concentrations of the gas stream and liquid stream. Peng-Rboinson equations of state were chosen for the equilibrium calculations.

Figure 17 shows the results of this calculation for the University of Hawaii's tests where corn starch and corn starch/poplar wood sawdust paste mixtures were fed to their reactor. The legend in Figure 17 shows the test conditions reported for these tests (Antal 1997 and Antal 1998). The x-axis contains the equilibrium mole fractions calculated by HYSIM (on a dry basis). The y-axis contains the measurements made at the University of Hawaii. The diamonds are the hydrogen mole fractions, the squares are the carbon dioxide mole fractions, the triangles are the carbon monoxide mole fractions, the circles are the methane mole fractions and the x's are the ethane mole fractions. Note that the equilibrium mole fraction for ethane at these conditions was zero.

The data in Figure 17 show that the hydrogen mole fractions measurements fall on both sides of the equilibrium concentration. Furthermore, the tests where the hydrogen is below the equilibrium concentration are the same tests where the methane is above the equilibrium concentration. Clearly in these tests, methane is being formed at the expense of the hydrogen yield.

Figure 18 shows a plot of the hydrogen yield, in liters/g of solids feed as a function of the peak reactor temperature. Tests 4, 5 and 6 are not shown on this graph because the total gas yield was not reported for these tests. The peak reactor temperature is usually the temperature measured under the middle of the entrance heater block, and would be indicative of the heating rate of the fluid. This figure shows that higher peak temperatures favor the formation of more hydrogen gas. However, there is a considerable amount of scatter in the data. Tests 8 and 11, for example, show essentially the same hydrogen yield at drastically different peak reactor temperatures, while Tests 8 and 10 show drastically different hydrogen yields at the same peak reactor temperature. It is possible that these tests were conducted at different annulus heater power settings, which were not reported. The heat transfer model showed that the annulus heater power would affect the heating rate of the fluid. However, another explanation for these anomalies is that the wall seasoning phenomena that Antal (1987) discusses.

Figure 19 shows a plot of the predicted equilibrium mole fractions as a function of the concentration of wood feed to the reactor at 600 °C. In this simulation, only wood and water were assumed to be in the feed stream (no corn starch). This figure shows that increasing the concentration of biomass in the feed stream will result in less hydrogen and more methane formation, if the reaction is allowed to go to completion. This will be an important consideration in a commercial process, as lower wood concentrations will increase the quantity of energy required to gasify the same amount of biomass.

Conclusions

The Heat Transfer Model provides some valuable insight into the temperature profiles within the University of Hawaii's Supercritical Water Reactor. Data with corn starch and wood/corn starch pastes indicates that there are substantial differences in the fluid properties of the pastes as compared to those of pure water particularly near the pseudo-critical temperature. The assumption of constant thermal diffusivity in the temperature range of 250 to 450 °C gives a reasonable prediction of the reactor temperatures when paste is being fed.

The results of the literature review and an analysis of the University of Hawaii's data indicate that the hydrogen yield will be favored by higher heating rates of the wood, higher reactor temperatures and shorter residence times, assuming that the secondary gasification reactions produce hydrogen concentrations in excess of equilibrium of the tertiary reactions. Furthermore, equilibrium considerations indicate that higher wood concentrations in the feed stream will favor the formation of methane over hydrogen.

At this time, there is insufficient data to develop a comprehensive kinetic model of the supercritical water biomass pyrolysis process. However, a global model based on the pathways described above and calibrated with kinetic data in the literature may be possible. Such a model would, hopefully, lead to a better understanding of the process and might explain some of the observations that are presently not fully understood, such as the wall seasoning effect.

Acknowledgments

This work was funded by the Department of Energy and the National Renewable Energy Laboratory (AXE-8-17103-01). We are particularly grateful to Dr. Michael Antal, Jr. of the University of Hawaii for allowing us to use his data and for his assistance on this project.

References

Antal, M. J. Jr., and X. Xu, 1997, "Total Catalytic Supercritical Steam Reforming of Biomass", 1997 Annual Report for Coop. Agreement DE-FG36-94AL85804.

Antal, M. J. Jr., 1998, "Hydrogen Production from Biomass in Supercritical Water", Quarterly Progress Report for Coop. Agreement DE-FG36-94AL85804, January-March 1998.

Bobleter, O., 1994, "Hydrothermal Degradation of Polymers derived from Plants", in *Prog. Polym. Sci.*, Vol. 19, 797-841.

Chapra, S. C., and R. C. Canale, 1988. *Numerical Methods for Engineers*, Second Edition, McGraw Hill Book Company.

Holgate, H. R. and J. W. Tester, 1994. "Oxidation of Hydrogen and Carbon monoxide in sub-and Supercritical water: Reaction kinetics, Pathways, and Water Density Effects: 2. Elementary Reaction Modeling", *J. Phys. Chem.*, **98** (3), 810.

Holgate, H. R., J. C. Meyer, and J. W. Tester, 1995 "Glucose Hydrolysis and Oxidation in Supercritical Water", *AIChE Journal*, **41**, 3 (March), 637.

Marshall, W. L.; Frank, E. U., 1981, "Ion Product of Water Substance, 0-1000 °C, 1-10,000 Bars New International Formulation and Its Background", *J. Phys. Chem. Ref. Data,* **10**, 295.

Patankar, S. V., 1980. *Numerical Heat Transfer and Fluid Flow*, McGraw Hill Book Company.

Sarakanen, K. V. and L. H. Hoo, 1981, J. Wood Chem. Technol., **1**, 11.

Schwald, W. and O. Bobleter, 1989, *J. Carbohydrate Chem.*, **8**, 565.

Sircar, S. 1998, "Sorption Enhanced Reaction (SER) for Production of Hydrogen", presented at the 1998 Hydrogen Program Annual technical Review meeting, Project Number DE-FC36-956010059.

Webley, P. A.; Tester, J. W., 1991, "Oxidation of Methane in Supercritical Water" *Energy & Fuels*, **5**, 411.

West, M. A. B. and M. R. Gray, 1987, "Pyrolysis of *1,3*-Butanediol as a Model Reaction for Wood Liquefaction in Supercritical Water", Canadian Journal of Chemical Engineering, **65**, August, 645.

Xu, X., Matsumura, Y., Steinberg, J. and Antal, J. A., Jr., 1996, "Carbon Catalyzed Gasification of Organic Feedstocks in Supercritical Water", *Industrial & Engineering Chemistry Research*, Vol. **35**, No. 8, 2522.

Figure Titles

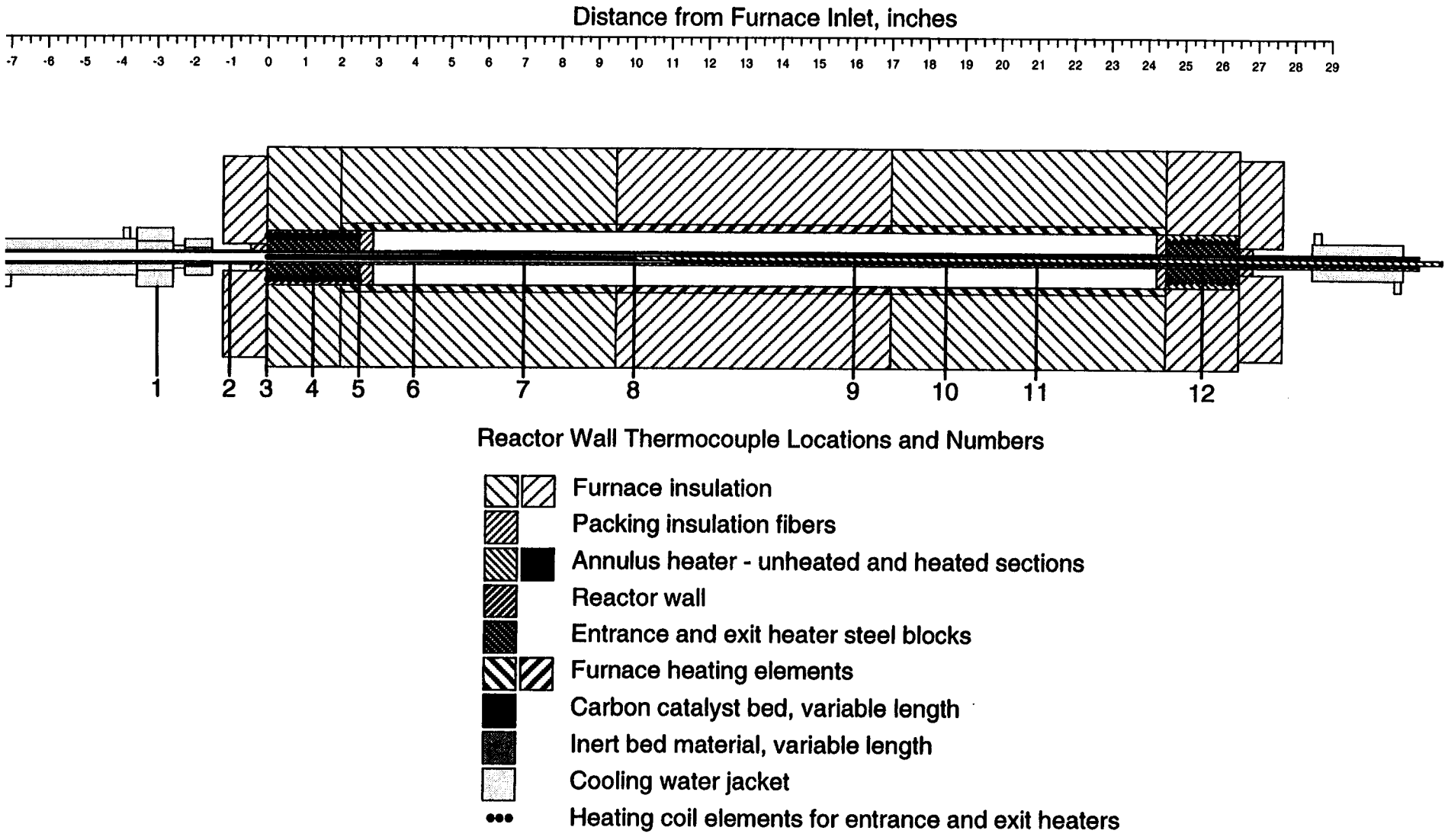

Figure 1. Overall Configuration of the University of Hawaii's SCW Reactor.

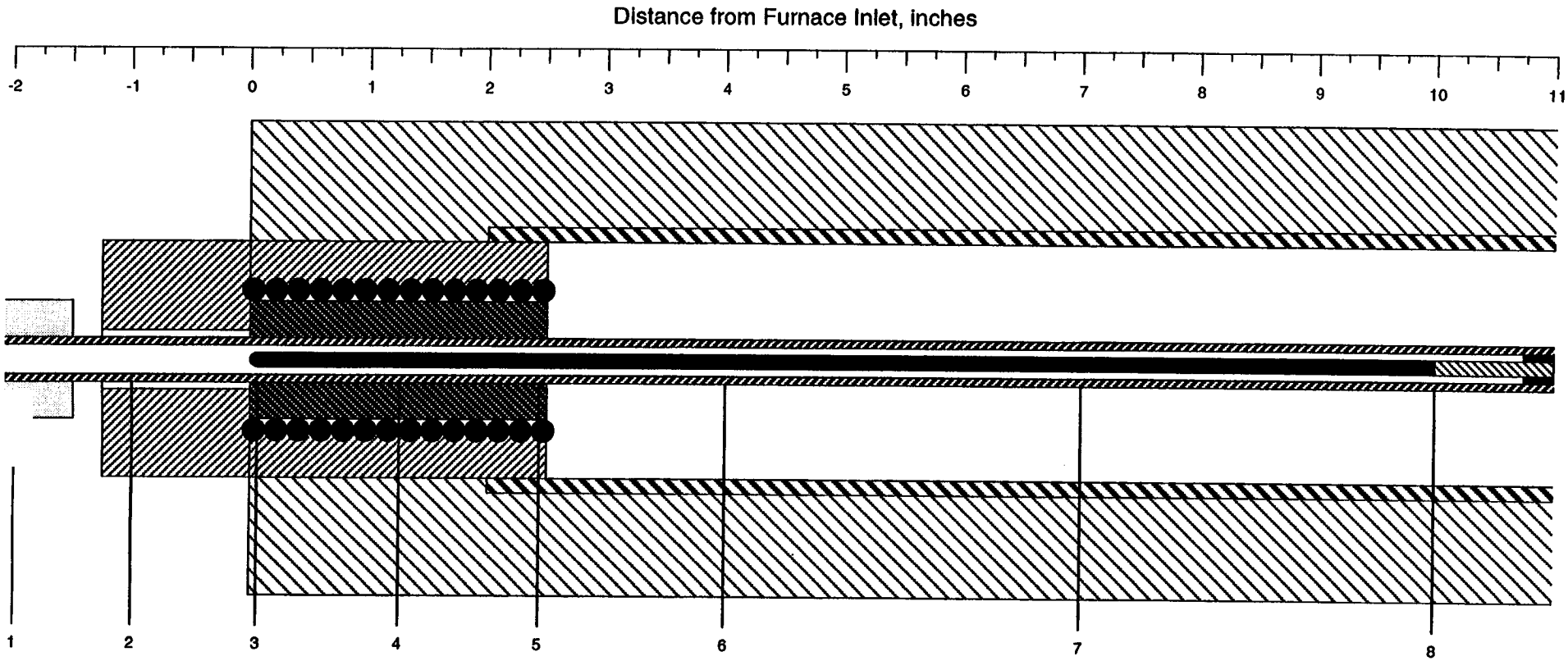

Figure 2. Entrance Heater Details.

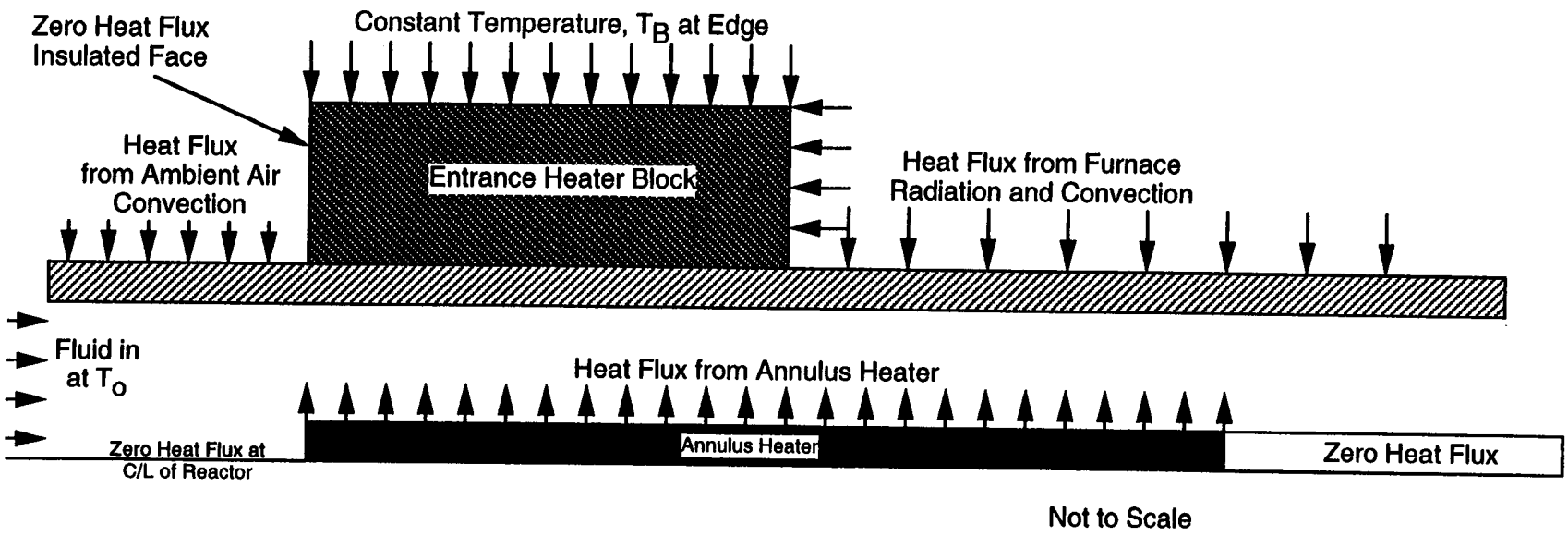

Figure 3. Boundary Conditions for Heat Transfer Model.

Figure 4. Heat Transfer Test Results at the University of Hawaii's SCWR.

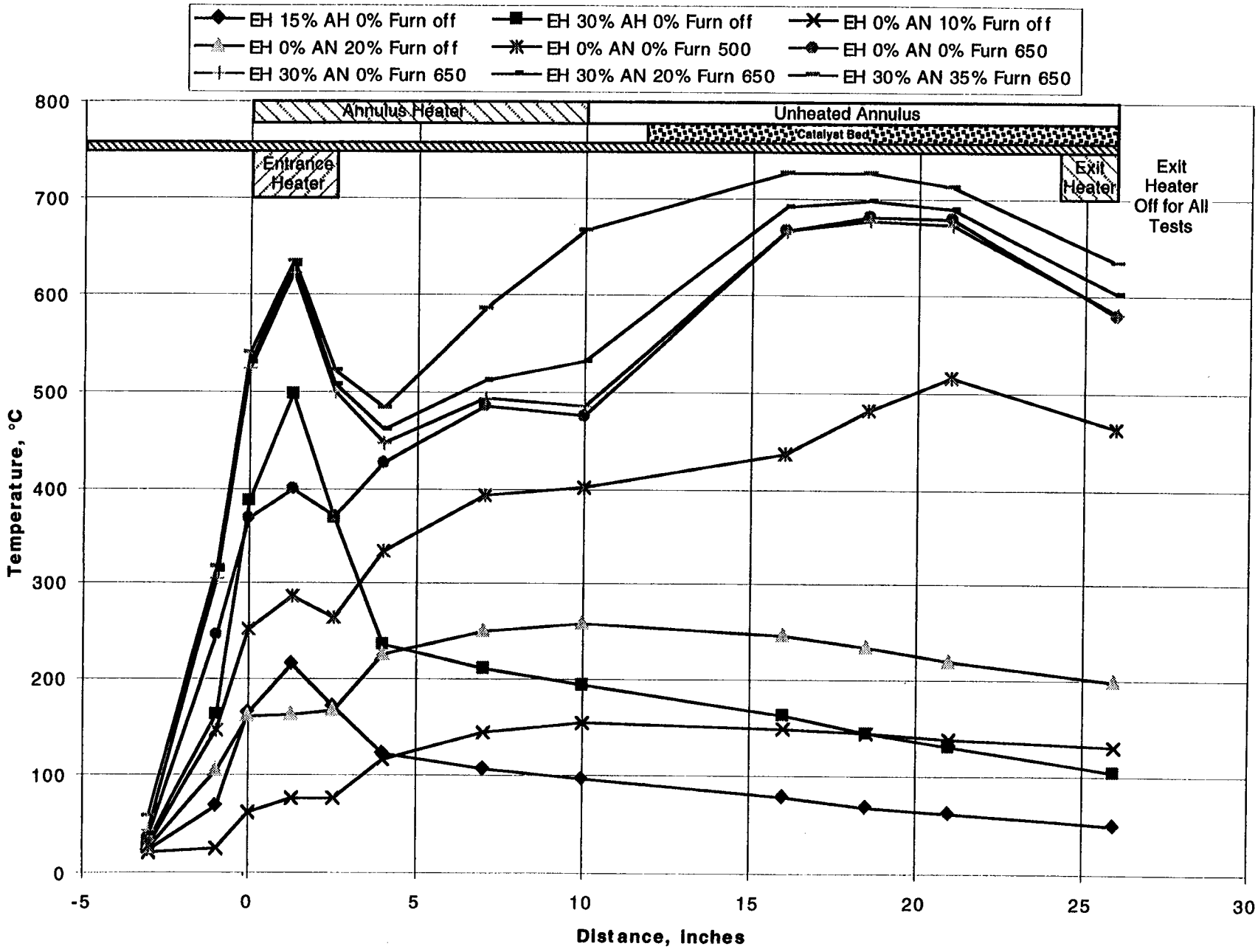

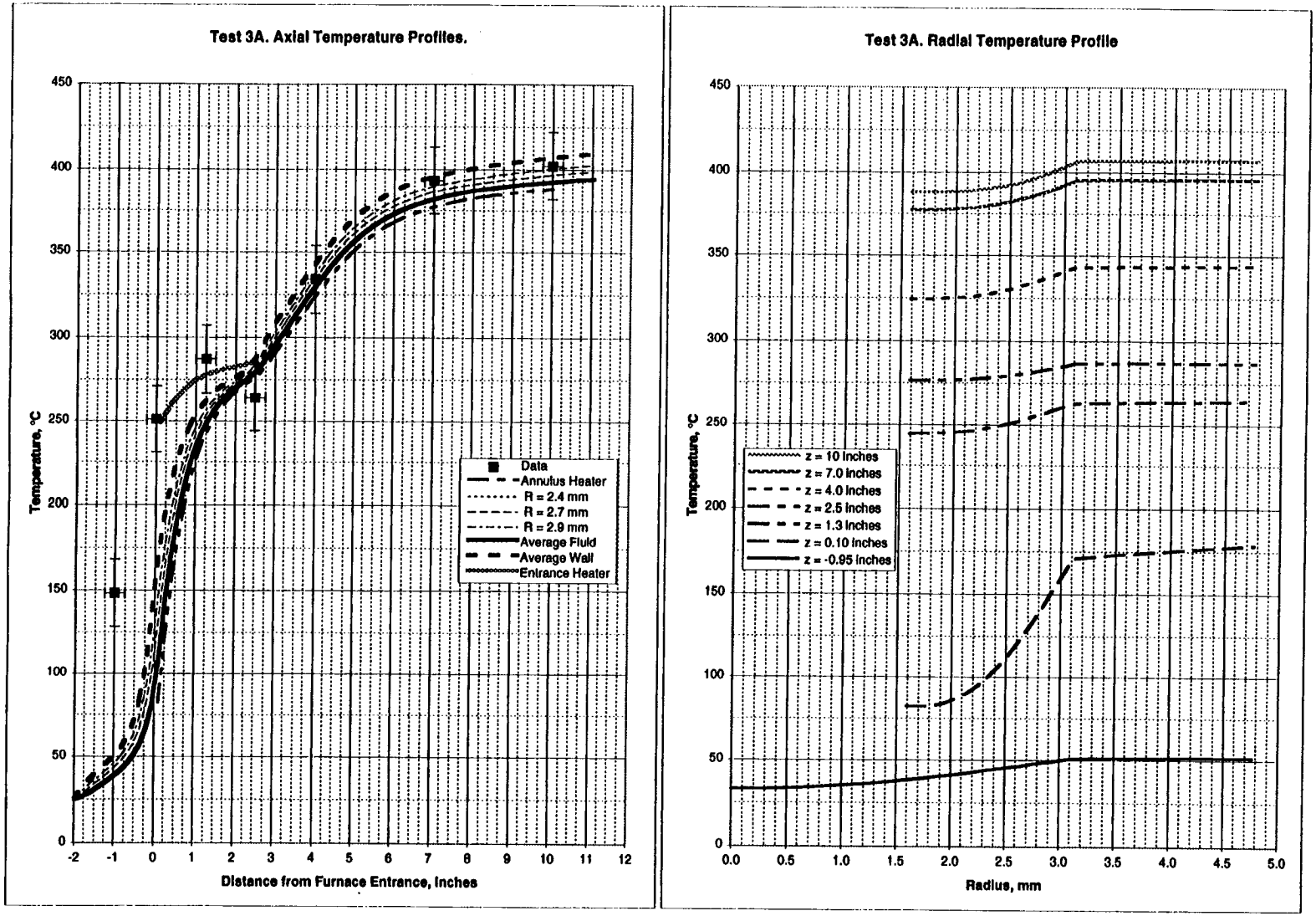

Figure 5. Test 3A Calculated Axial and Radial Temperature Profiles.

Entrance Heater 0% - Annulus Heater 0% - Furnace 500 °C

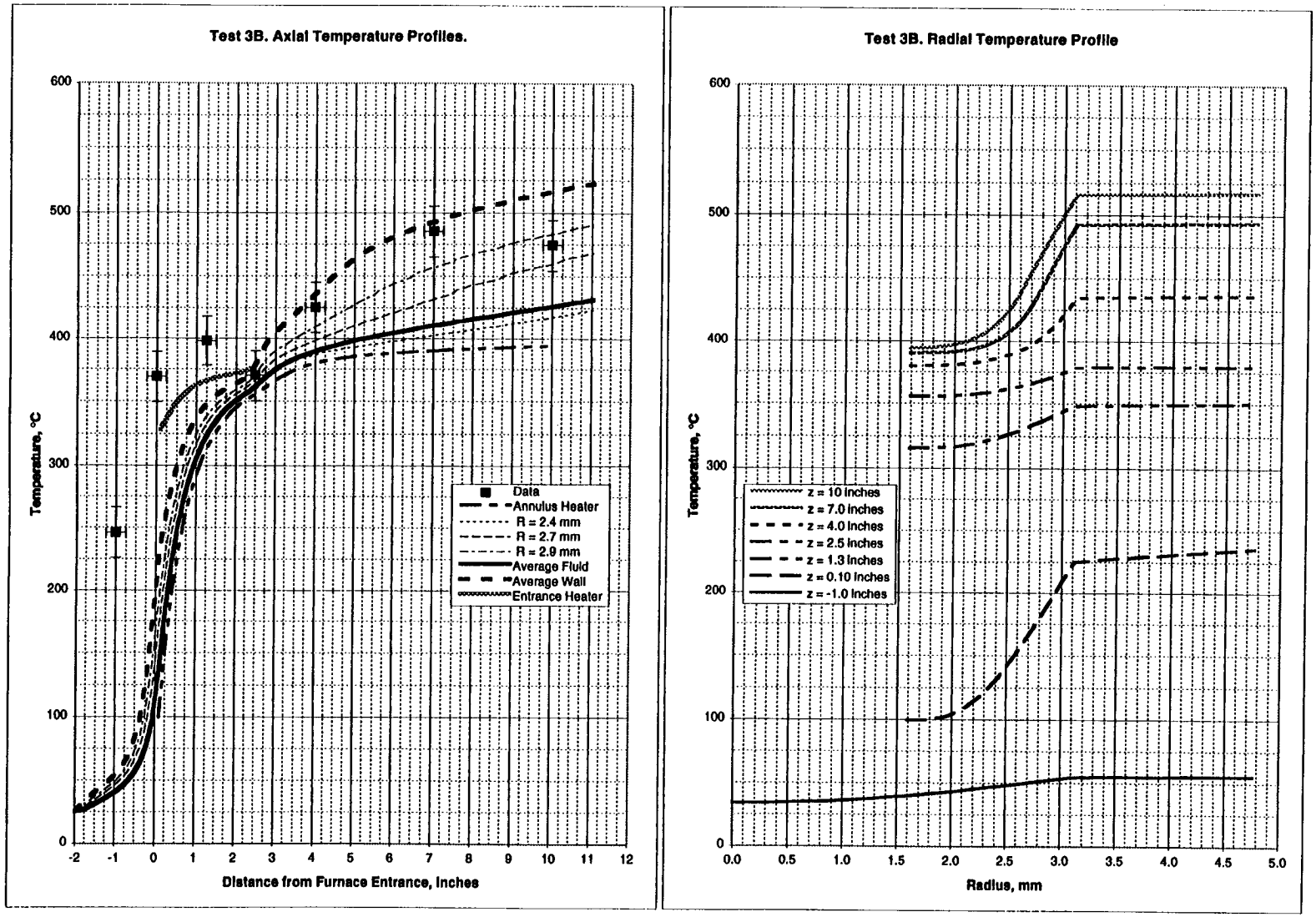

Figure 6. Test 3B Calculated Axial and Radial Temperature Profiles.

Entrance Heater 0% - Annulus Heater 0% - Furnace 650 °C

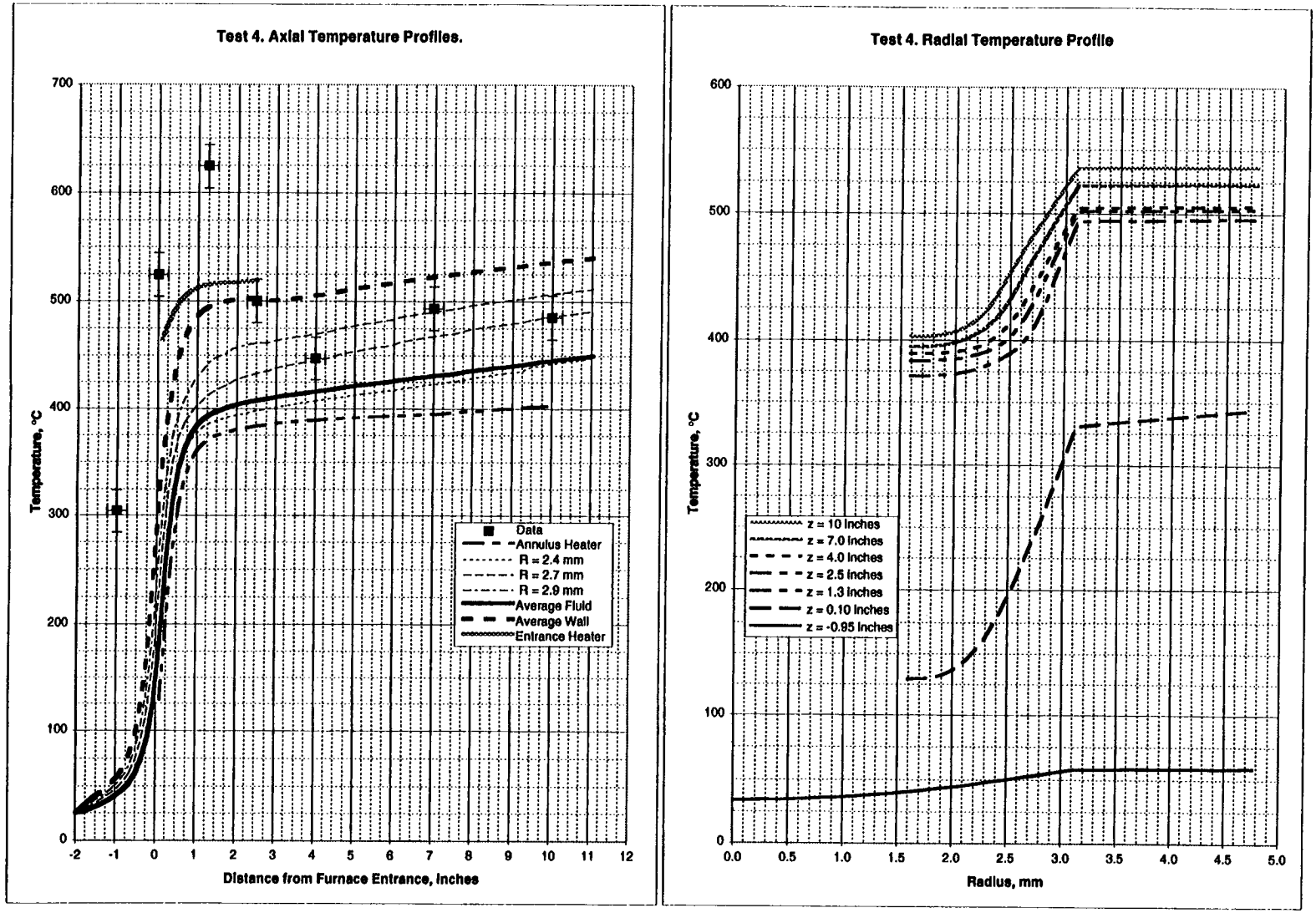

Figure 7. Test 4 Calculated Axial and Radial Temperature Profiles.

Entrance Heater 30% - Annulus Heater 0% - Furnace 650 °C

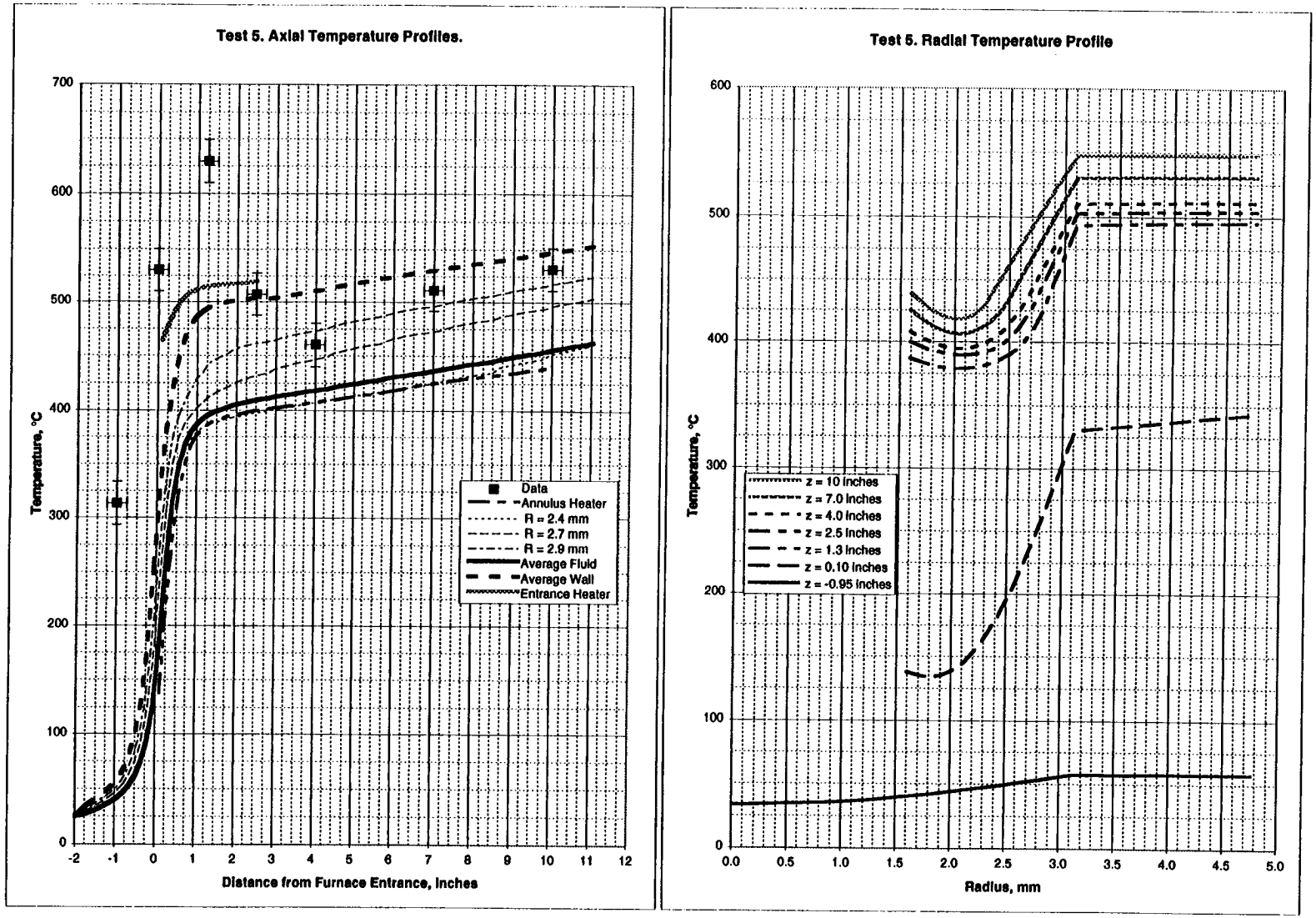

Figure 8. Test 5 Calculated Axial and Radial Temperature Profiles.

Entrance Heater 30% - Annulus Heater 20% - Furnace 650 °C

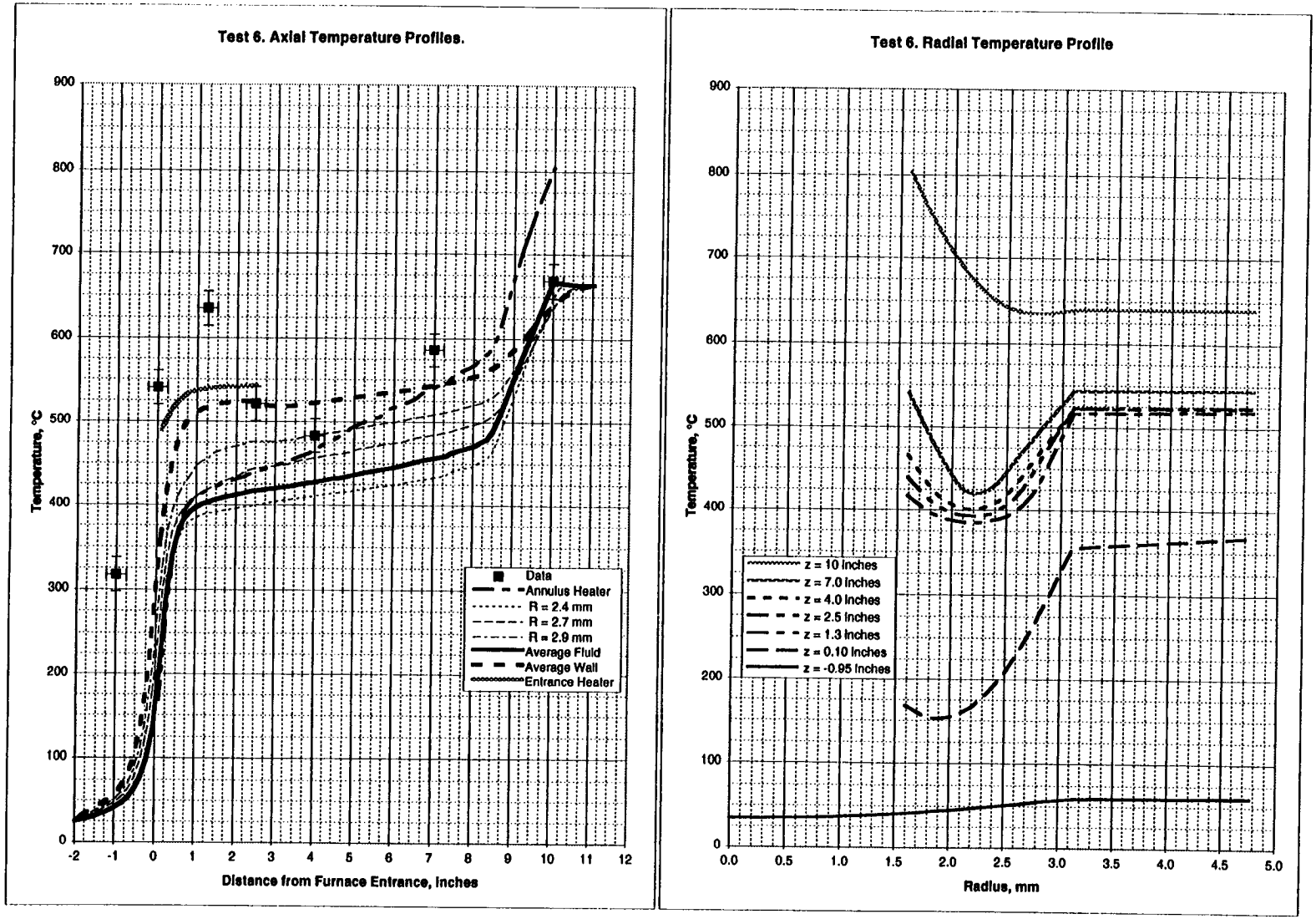

Figure 9. Test 6 Calculated Axial and Radial Temperature Profiles.

Entrance Heater 30% - Annulus Heater 35% - Furnace 650 °C

Figure 10. Watts Required to Heat Water up to a Desired Temperature at 28 MPa

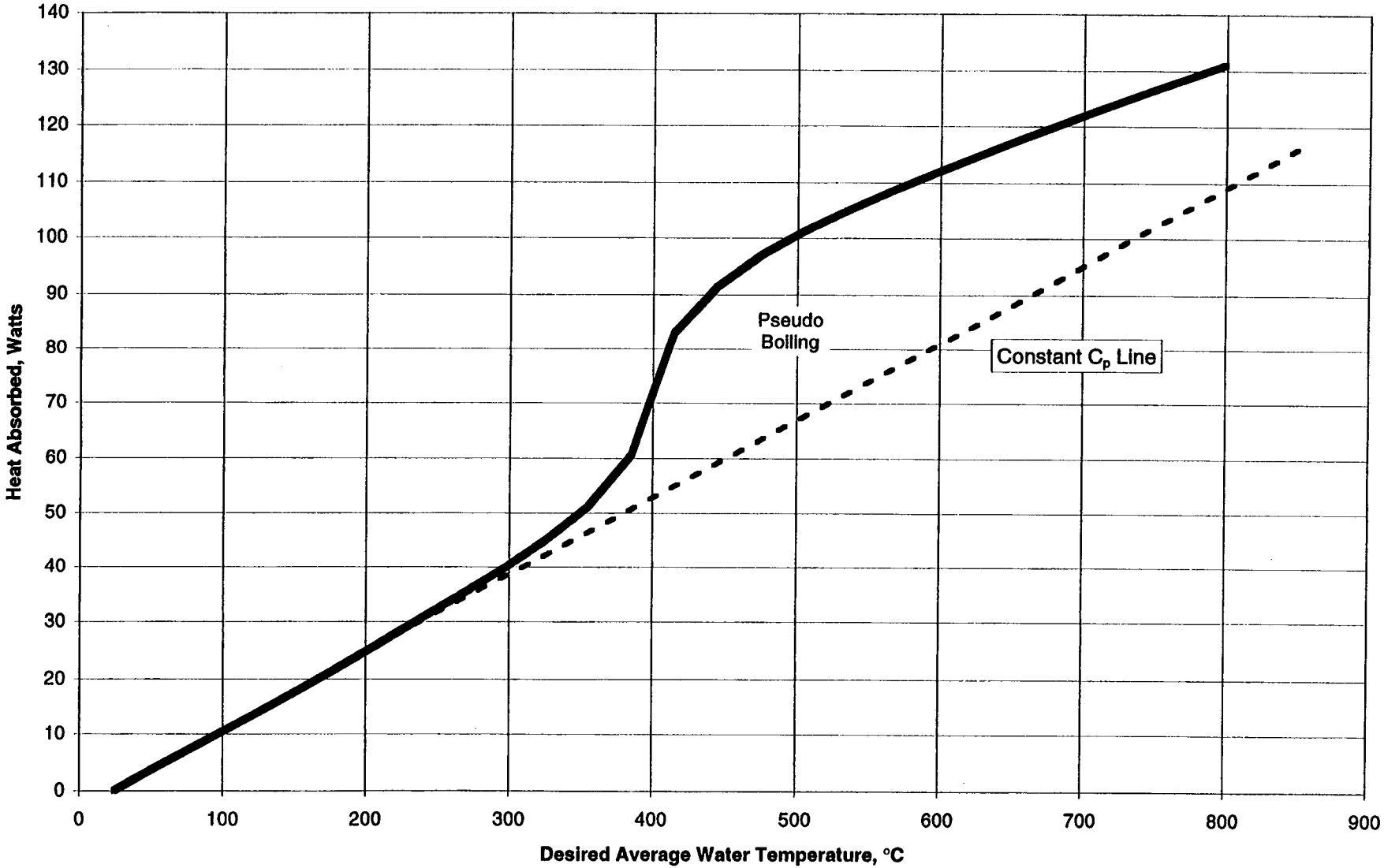

Figure 11. Axial Wall Temperature Profiles in New Reactor on 12/29/97

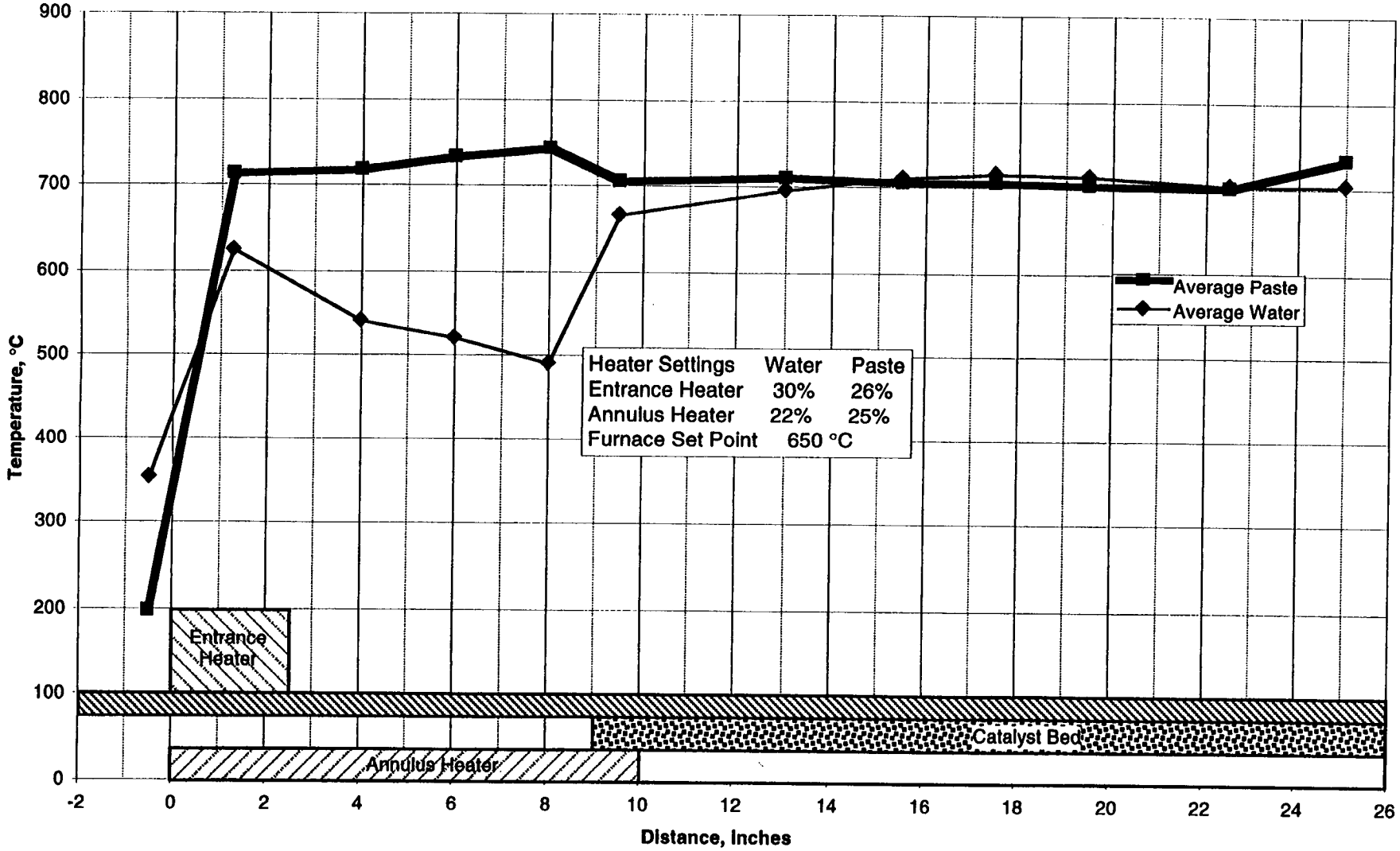

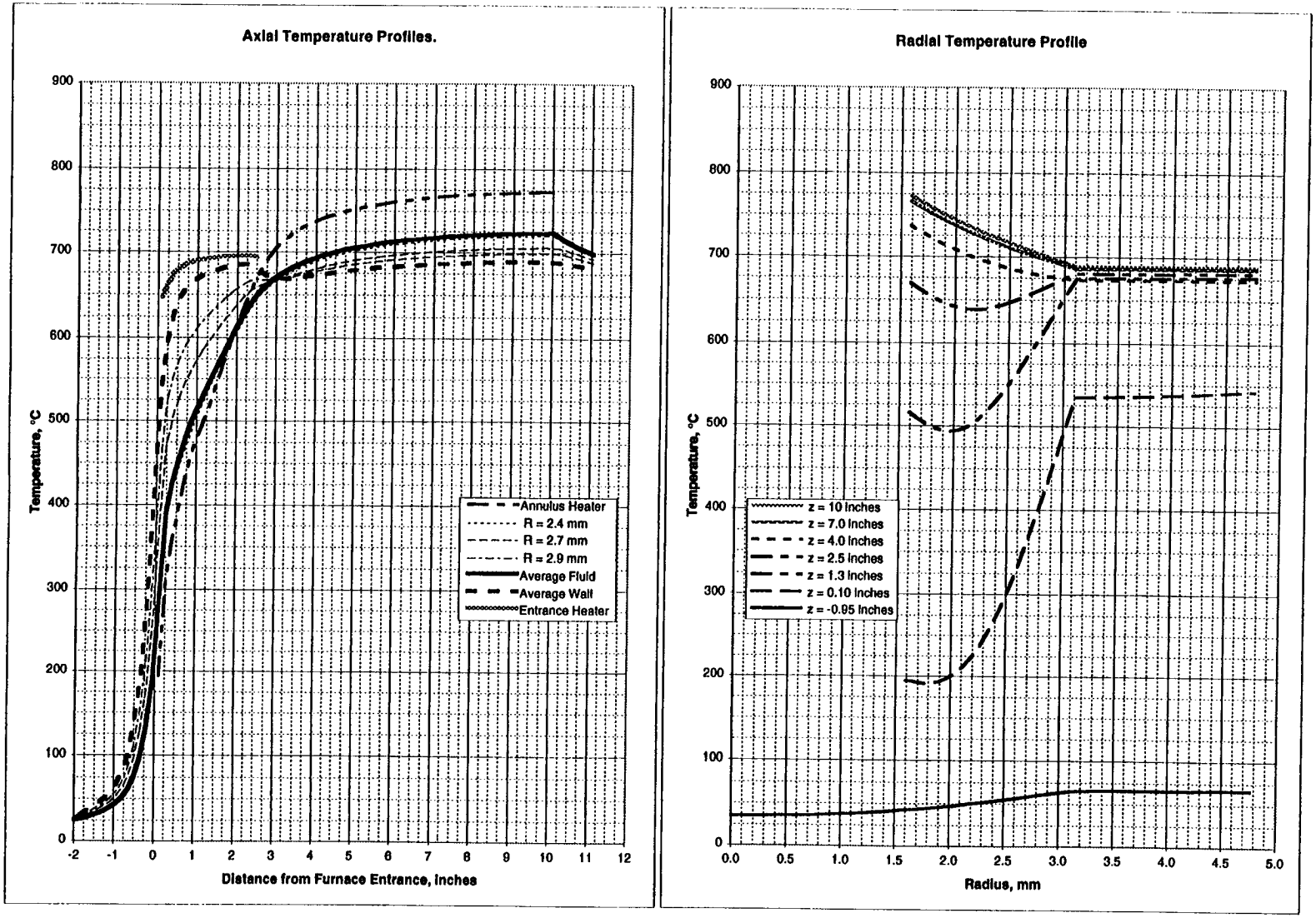

Figure 12. Calculated Axial and Radial Temperature Profiles for Wood Paste.

Entrance Heater 30% - Annulus Heater 20% - Furnace 650 °C

Figure 13. Predicted Temperature versus Time for Wood Paste
Entrance Heater 30% - Annulus Heater 35% - Furnace 650 °C

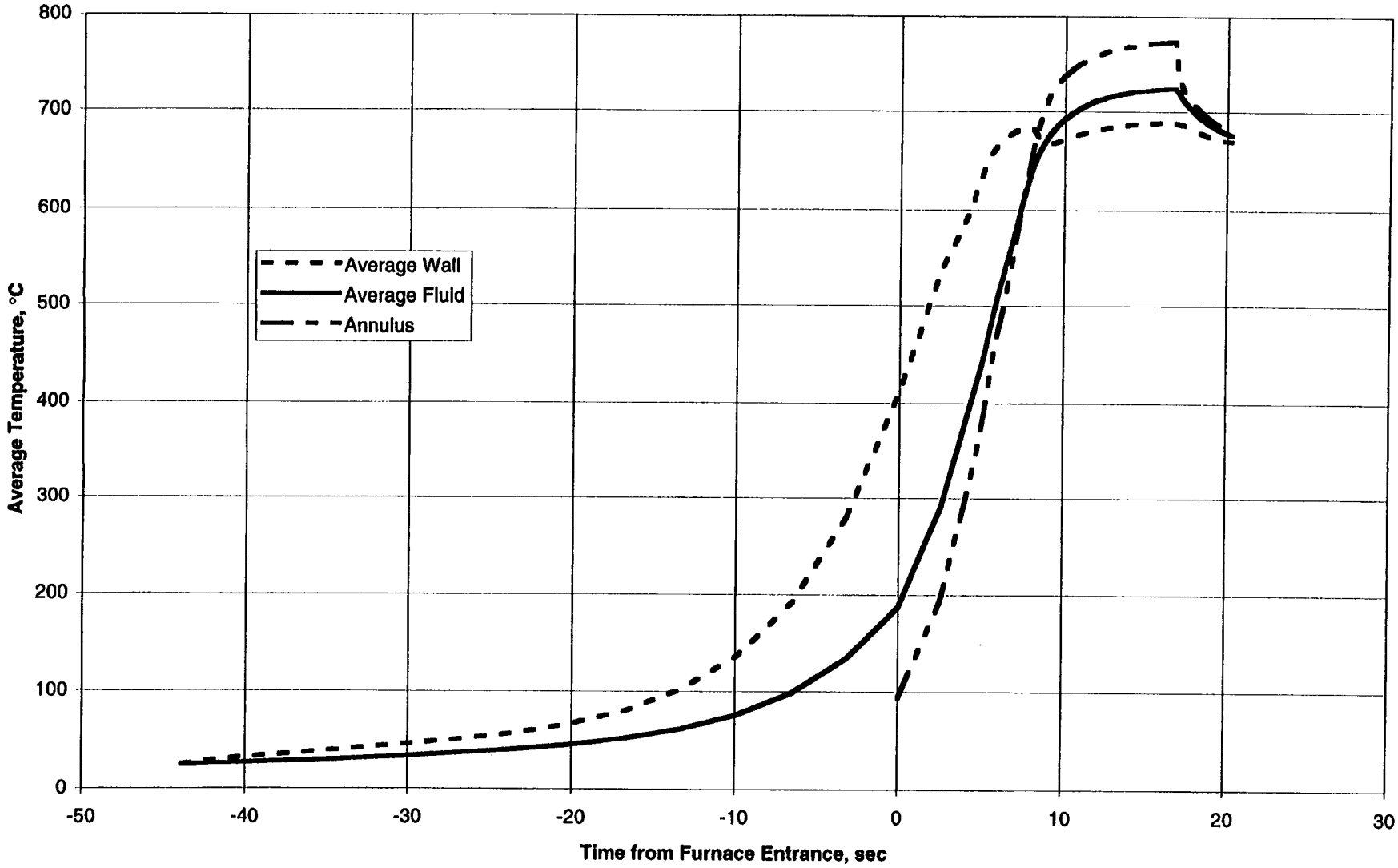

Figure 14. Hydrogen Ion Concentration in Pure Water versus Temperature

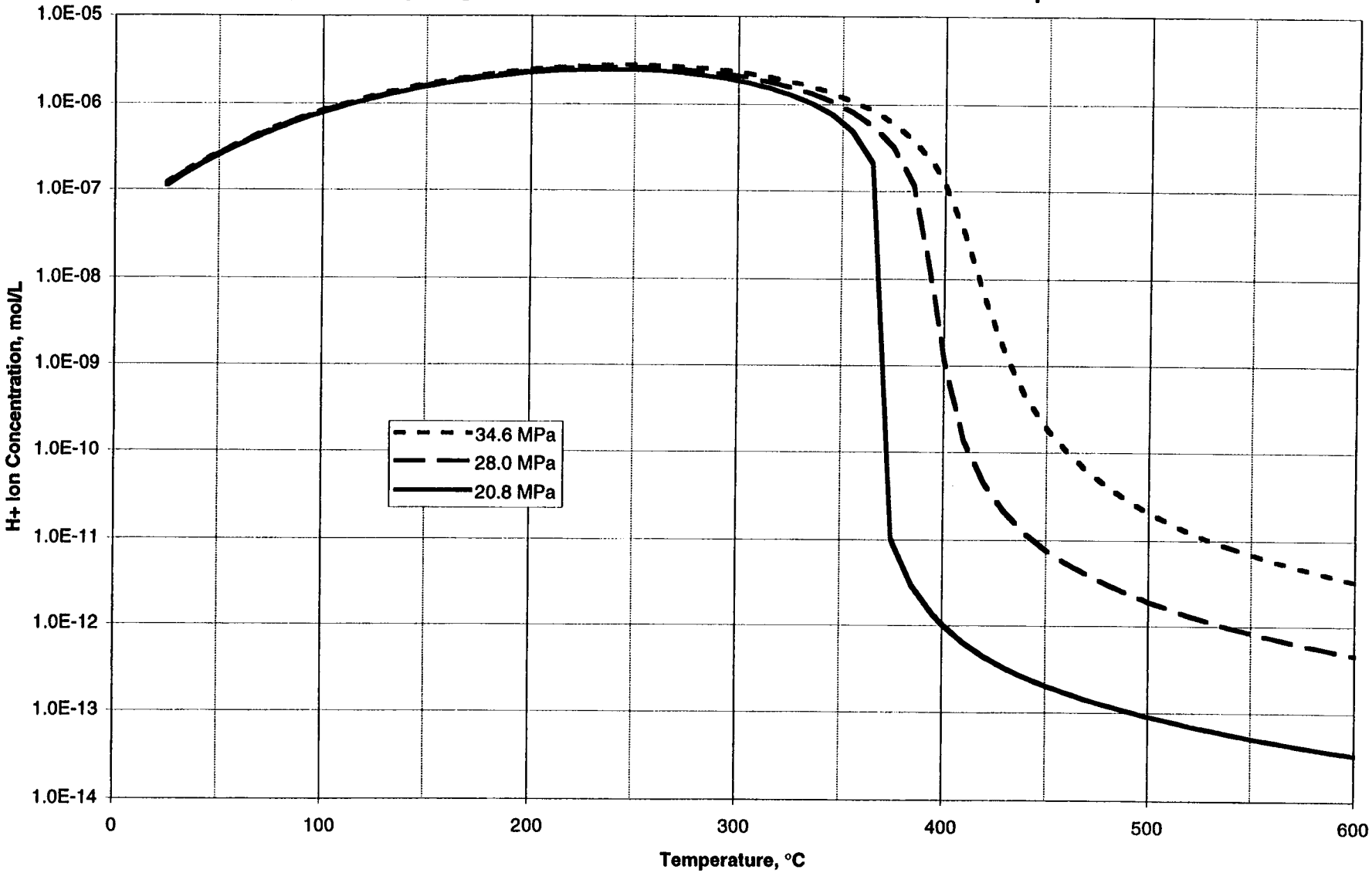

Source: Marshall and Frank, J. Phys. Chem. Ref. Data, Vol 10, No. 2, 1981, P 295-304.

Figure 15. Holgate & Tester (1995) Data Major Pyrolysis Products of 0.001M Glucose in SCW.

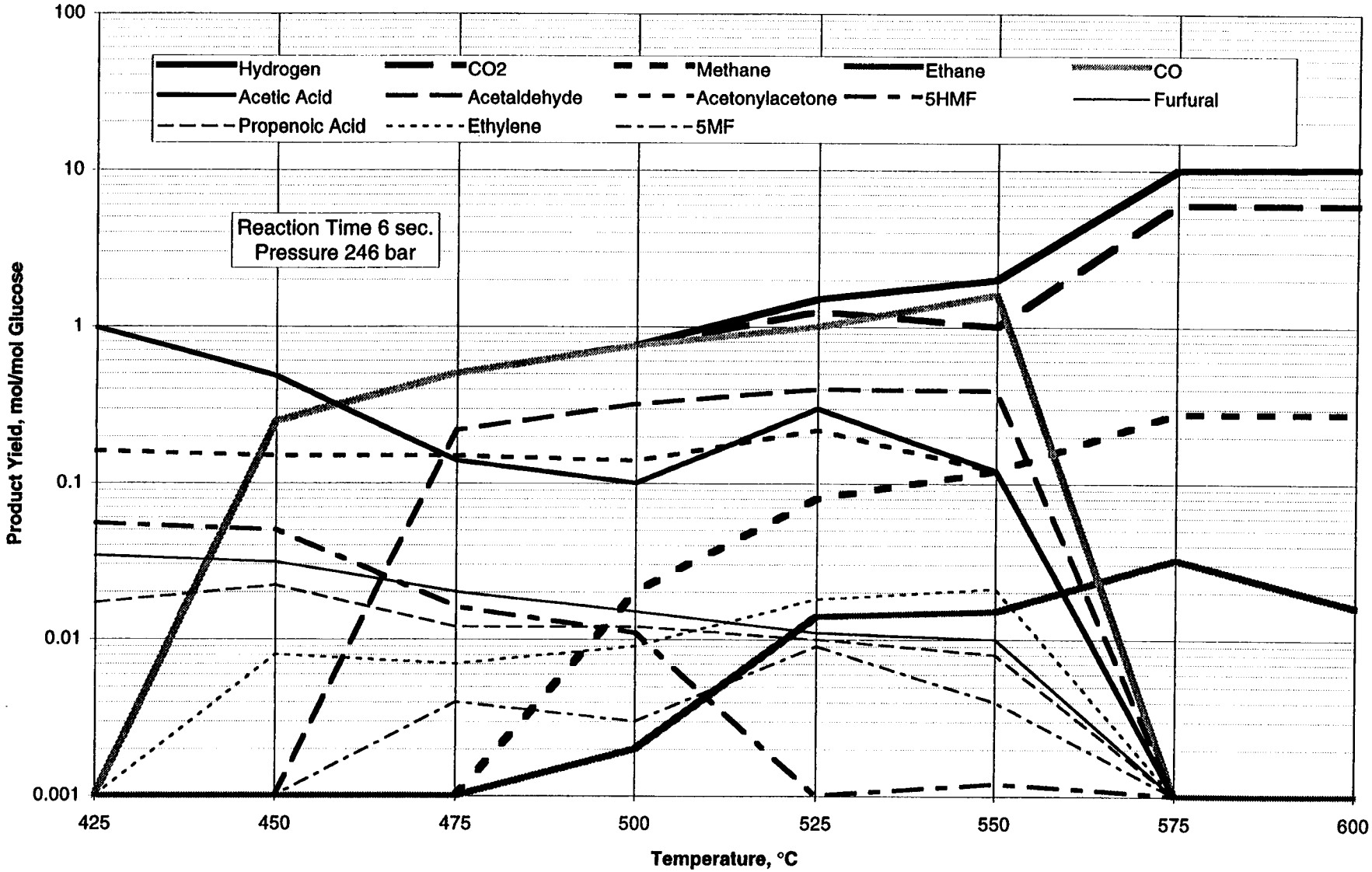

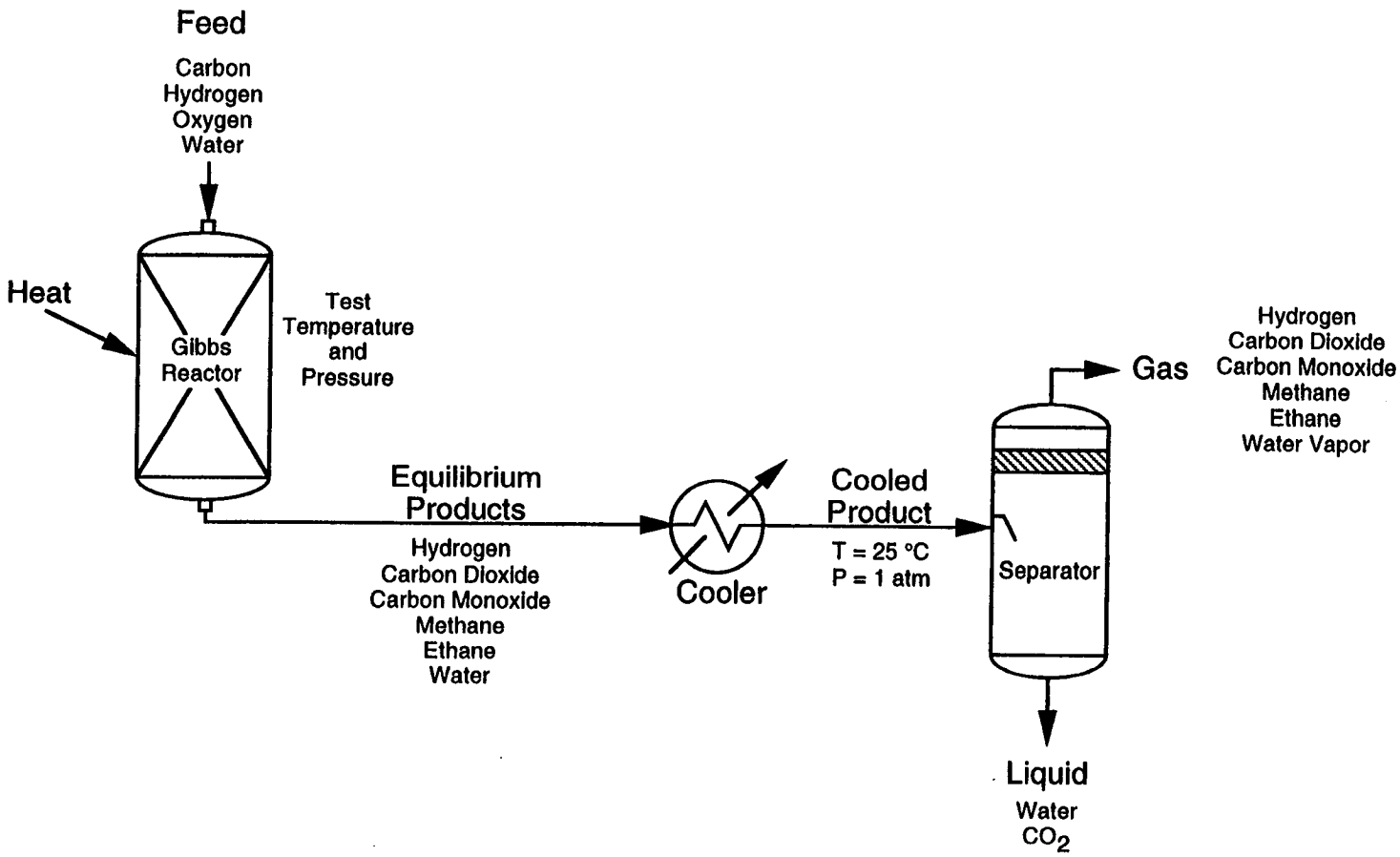

Figure 16. HYSIM Simulation of the University of Hawaii's SCW Reactor.

Figure 17. Comparison of Test Measurements to Equilibrium at Catalyst Temperature.

Point No.	Test Date	Flow Rate, g/min	Wt.% Corn Starch	Wt. % Poplar Wood	Catalyst Temp. °C	Peak Temp. °C
1	20-Feb-97	1.0	10.40	0.00	650	690
2	20-Feb-97	2.0	10.40	0.00	650	715
3	20-Feb-97	4.0	10.40	0.00	650	805
4	25-Mar-97	2.0	5.50	5.00	640	890
5	25-Mar-97	2.5	5.50	5.00	640	900
6	23-Apr-97	2.0	5.55	5.00	650	785
7	1-May-97	2.0	6.09	5.05	630	700
8	3-Jul-97	2.0	4.01	10.72	685	790
9	10-Jul-97	2.0	4.19	11.17	700	790
10	10-Jul-97	2.0	4.19	11.17	700	790
11	21-Jul-97	2.0	4.15	11.10	690	732
12*	21-Aug-97	2.0	4.13	11.08	690	730
13	29-Aug-97	2.0	4.11	11.35	685	770
14	5-Sep-97	2.0	4.19	11.76	690	800
15**	17-Dec-97	2.0	3.55	9.47	700	750
16**	12-Feb-98	2.0	3.65	10.04	700	725

* 1/16" OD annulus used for this test.
** New Reactor Configuration

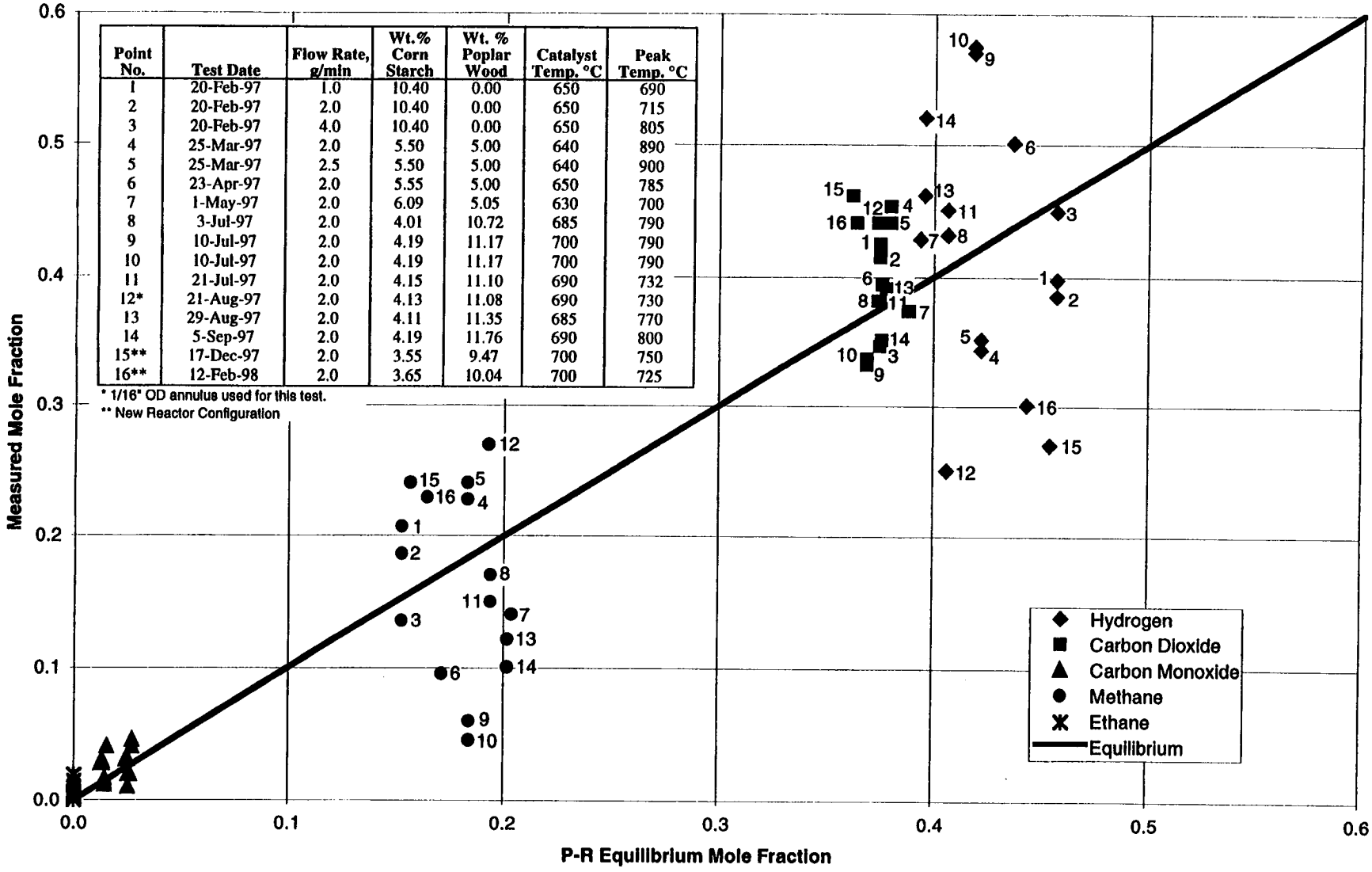

Basis: HYSIM Equilibrium Calculation using Peng-Robinson Equations of State

Figure 18. Hydrogen Yield versus Peak Temperature for Wood Paste Tests

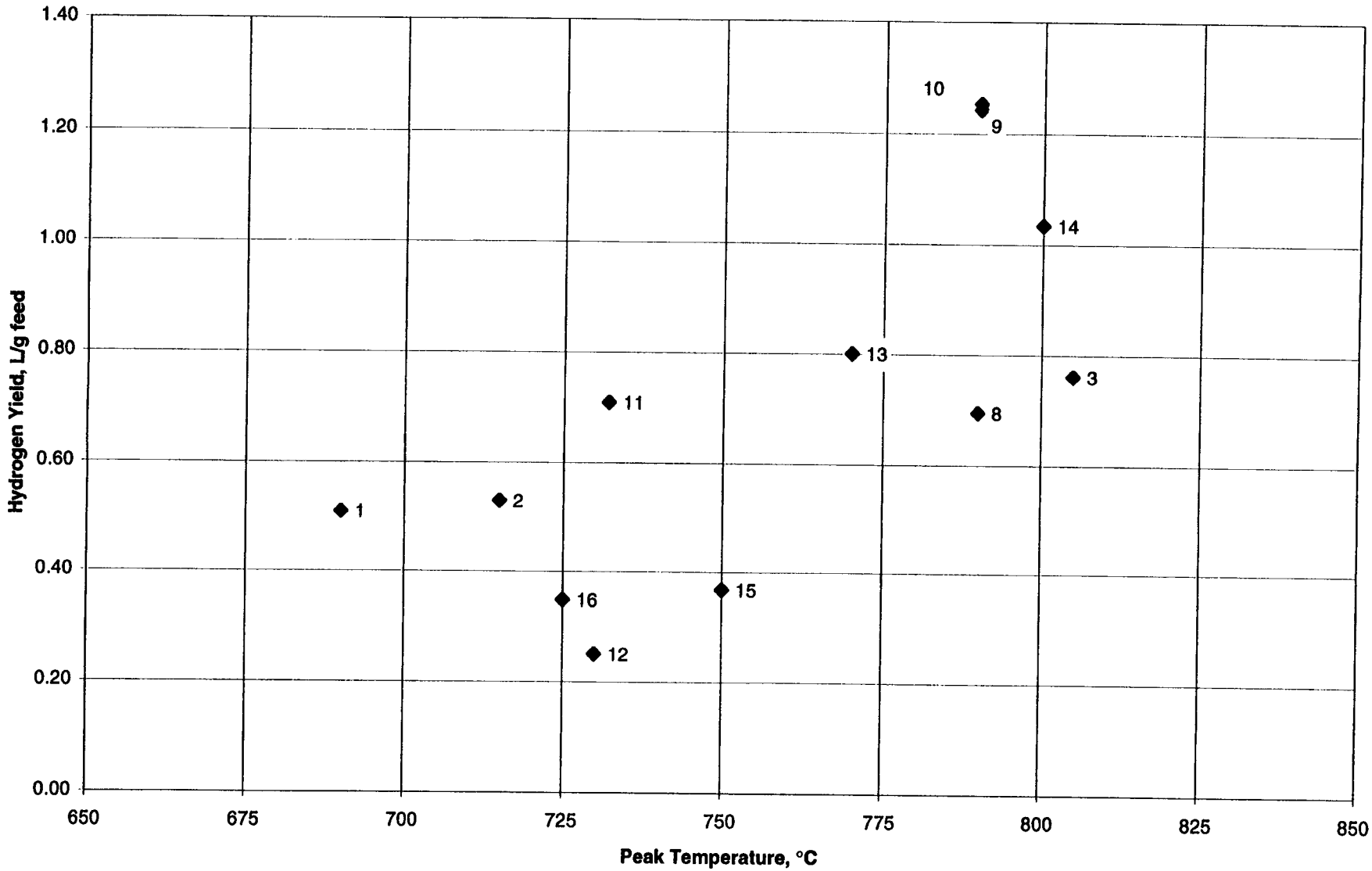

Figure 19. Equilibrium Mole Fractions versus Percent Wood in the Feed at 600 °C.

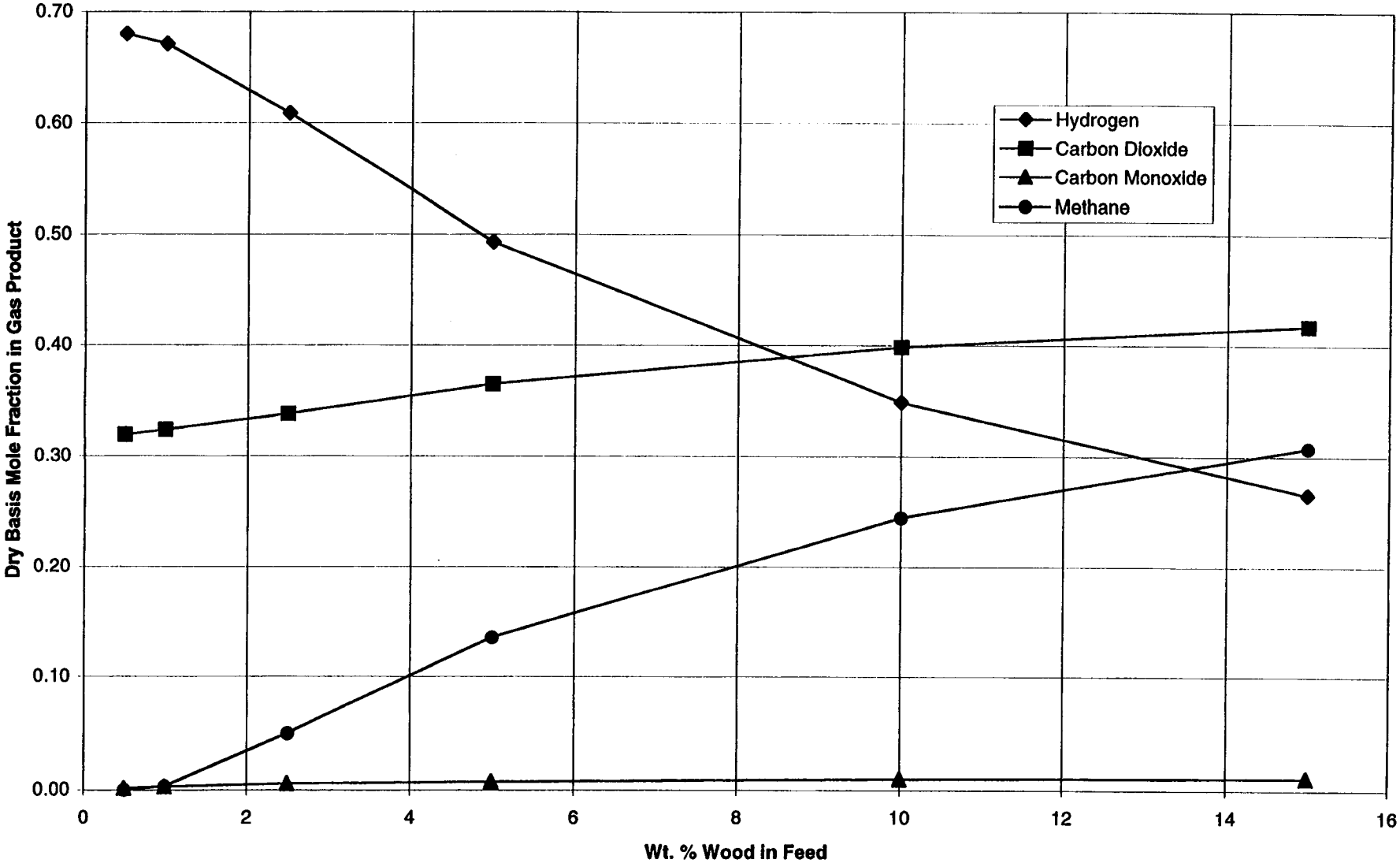

Basis: HYSIM Equilibrium Calculation using Peng-Robinson Equations of State